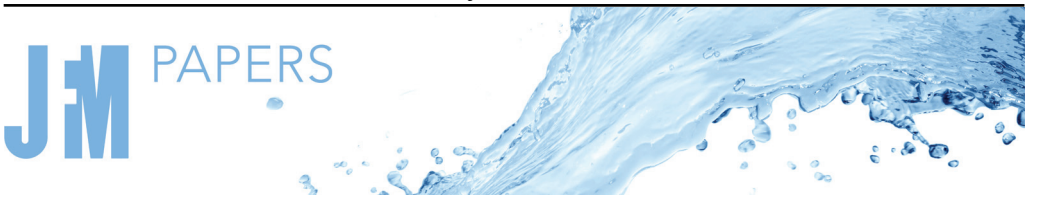
J. Fluid Mech. (2025), *vol.* 1025, A64, doi:10.1017/jfm.2025.10998



How boundary layer flows influence cavitation bubble-driven particle jumps from rigid walls

Zibo Ren[1], **Wenchao Zhang**[2,3], **Qingyun Zeng**[2,3], **Zhigang Zuo**[1] and **Shuhong Liu**[1]

[1]State Key Laboratory of Hydro Science and Engineering, and Department of Energy and Power Engineering, Tsinghua University, Beijing 100084, PR China

[2]College of Shipbuilding Engineering, Harbin Engineering University, Harbin 150001, PR China

[3]Nanhai Institute of Harbin Engineering University, Sanya 572024, PR China

Corresponding authors: Zibo Ren, rzb18@tsinghua.org.cn; Zhigang Zuo, zhigang200@tsinghua.edu.cn; Shuhong Liu, liushuhong@mail.tsinghua.edu.cn

(Received 15 August 2025; revised 3 November 2025; accepted 25 November 2025)

The interaction between cavitation bubbles and particles near rigid boundaries plays a crucial role in applications from surface cleaning to cavitation erosion. We present a combined experimental, numerical and theoretical investigation of how boundary layer flows affect particle motion during the growth and collapse of the cavitation bubble. Using laser-induced cavitation bubbles and particles of varying radius ratios and stand-off distances, we observe that increasing the bubble-to-particle size ratio suppresses particle displacement. Through one-way coupled simulations and theoretical modelling, we demonstrate that this suppression arises from a shift in the dominant forces acting on the particle: for small radius ratios, the pressure gradient force governs particle motion, while for large ratios, the interplay between added mass, lubrication, and pressure gradient forces becomes significant due to boundary layer growth in the bubble-induced stagnation flow. Based on a theoretical framework combining potential flow theory and axisymmetric viscous stagnation flow analysis, we identify the inviscid- and viscous-flow dominated regimes characterised by the combination of the stand-off distance, the bubble-to-particle radius ratio, and the bubble Reynolds number. Finally, we derive scaling laws for particle displacement consistent with experiments and simulations. These findings advance our understanding of unsteady boundary layer effects in cavitation bubble-particle interactions, offering new insights for applications in microparticle manipulation and flow measurements.

Key words: bubble dynamics, cavitation, particle/fluid flows

© The Author(s), 2025. Published by Cambridge University Press.

https://doi.org/10.1017/jfm.2025.10998 Published online by Cambridge University Press

1. Introduction

Cavitation, the generation, growth and collapse of vapour bubbles in a liquid due to a pressure drop below the saturated vapour pressure, plays a significant role in various engineering applications and natural phenomena (Brennen 2014). In environments with high sediment loads, such as the Yellow River, cavitation bubbles interact with solid particles, leading to erosion damage on structures such as ship propellers, hydropower turbine blades, and spillway walls (Arndt 1981; Karimi & Martin 1986). Conversely, this interaction can be harnessed for beneficial purposes, including ultrasonic cleaning of particle-contaminated surfaces (Bulat 1974), shock wave lithotripsy for kidney stone fragmentation (Zhong 2013; Xiang *et al.* 2023), and even powder preparation (Mordyuk & Prokopenko 2004; Dvorsky, Lunacek & Sliva 2011). Therefore, understanding the interaction between cavitation bubbles and solid particles near solid walls holds crucial importance for both mitigating detrimental effects and exploiting its potential for various technological advancements.

Prior research has extensively investigated the interaction between cavitation bubbles and particles. Early theoretical models linked this interaction to surface erosion (Li 2006). Pioneering experimental work by Arora, Ohl & Mørch (2004) employed shock waves from a lithotripter to observe the acceleration of micron-sized particles away from a growing bubble in water. This self-propelled motion suggested that particles might be accelerated towards walls during cavitation, potentially causing surface damage (Borkent *et al.* 2008). However, the limited controllability of shock waves for generating single cavitation bubbles led subsequent studies to utilise laser-induced (Lauterborn & Bolle 1975) or spark-induced cavitation bubbles (Harrison 1952) for more precise control of bubble size and position. Building on these advancements, Poulain *et al.* (2015) quantitatively studied the interaction between spark-induced cavitation bubbles and suspended particles of comparable sizes, finding that the collapsing cavitation bubble attracts the particle. They proposed a power-law relationship between the dimensionless particle velocity and the dimensionless cavitation bubble–particle distance (Poulain *et al.* 2015). However, the observed pendulum-like motion of suspended particles may not accurately reflect the behaviour in liquids with freely moving particles. Wu *et al.* (2017) systematically studied the interaction between laser-induced millimetre-sized cavitation bubbles and freely settling sub-millimetre-sized particles. Their work demonstrated that particles can be accelerated and ejected at velocities $\approx 60\ \mathrm{m\ s^{-1}}$ away from a growing cavitation bubble. Subsequent research has explored the effects of particles on bubble shape evolution (Li *et al.* 2018; Wang *et al.* 2023), and the interactions of single cavitation bubbles with multiple particles in a liquid far from solid walls (Chen *et al.* 2021; Zheng *et al.* 2023; Wang *et al.* 2024).

Cavitation bubbles near rigid solid walls exhibit non-spherical collapse, generating high-speed micro-jets directed towards the wall, a phenomenon known to contribute significantly to cavitation erosion (Benjamin & Ellis 1966; Lauterborn & Ohl 1997; Brujan *et al.* 2002). Upon impact, the jet creates stagnation and radial flow along the wall, leading to extremely high shear rates within the boundary layer. For millimetre-sized bubbles, these shear rates can reach 1×10^7–$1 \times 10^8\ \mathrm{s^{-1}}$ (Dijkink & Ohl 2008; Zeng *et al.* 2018*a*, 2022). This boundary layer shear can both accelerate stationary microparticles on the wall, enabling surface cleaning applications (Ohl *et al.* 2006; Gonzalez-Avila *et al.* 2011), and remove larger, initially stationary wall-bound particles through uneven pressure distribution during bubble collapse (Chahine *et al.* 2016). Recent studies explored the acceleration of free particles near walls by millimetre-sized bubbles, highlighting the roles of bubble growth, collapse, jetting and vortex rings in particle–wall interactions

https://doi.org/10.1017/jfm.2025.10998 Published online by Cambridge University Press

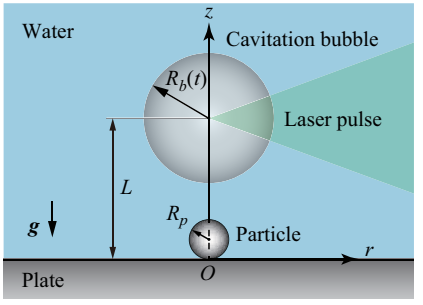


Figure 1. Schematic and notation of the core components of the experimental set-up in side view.

(Wu *et al.* 2021). Notably, Ren *et al.* (2022) reported a new phenomenon where millimetre-sized metal particles were propelled like projectiles from rigid walls by laser-induced bubbles of similar size, which was successfully explained with a potential flow model. However, the model neglected viscous effects, which are potentially significant at the finite Reynolds numbers associated with the maximum cavitation bubble radius to particle radius ratio greater than 1. In this paper, we address this gap by investigating the influence of viscous boundary layer flows on the cavitation-bubble-induced particle motion through experiments, simulations and theoretical analysis.

This paper is organised as follows. In § 2, we detail the experimental (§ 2.1) and numerical (§ 2.2) methods employed to investigate the cavitation bubble–particle interactions with different radius ratios and stand-off distances. In § 3, we present the experimental observations and numerical comparisons (§ 3.1), and discuss the evolution of hydrodynamic forces on the particle (§ 3.2) and the boundary layer flows induced by bubble oscillation (§ 3.3). Finally, in theory, we identify different dominant regimes for particle–bubble interactions and derive scaling laws for the particle's displacement that are comparable to the experiments and simulations (§ 3.4).

2. Methodology

2.1. *Experimental method*

Figure 1 presents a side view of the core components of the experimental set-up to study the interaction between laser-induced single cavitation bubbles and particles on a rigid boundary. A rectangular polymethylmethacrylate (PMMA) plate (size 100 mm × 50 mm × 10 mm) is horizontally submerged in a quartz container filled with deionised water and connected to a three-dimensional translation stage with accuracy 0.01 mm positioned outside the container using a support rod. A single particle is injected into the container through a fixed long thin tube from a syringe, which allows the particle to settle freely through the water onto the upper surface of the plate (Wu *et al.* 2017, 2021). Three types of spherical particles with varying sizes are used, i.e. PMMA particles with density $\rho_p = 1.18 \times 10^3\ \mathrm{kg\,m^{-3}}$ and radius $R_p = 250\ \mu\mathrm{m}$, PMMA particles with the same density and $R_p = 50\ \mu\mathrm{m}$ (both particles purchased from Suzhou Knowledge & Benefit Sphere Tech.), and polystyrene (PS) particles with $\rho_p = 1.05 \times 10^3\ \mathrm{kg\,m^{-3}}$ and $R_p = 25\ \mu\mathrm{m}$ (Beijing Zhongkeleiming Technology). The specific particle parameters are summarised in table 1.

With the translation stage, the particle is horizontally positioned below a single cavitation bubble generated by a Q-switched Nd:YAG laser (LPS-532-L, Changchun New Industries Optoelectronics Technology, wavelength 532 nm, maximum pulse energy

https://doi.org/10.1017/jfm.2025.10998 Published online by Cambridge University Press

Particle material	Density ρ_p (kg m^{-3})	Radius R_p (μm)	Radius ratio $R_{b,max}/R_p$
PMMA	1.18×10^3	250	1.6–4.0
PMMA	1.18×10^3	50	8–20
PS	1.05×10^3	25	16–40

Table 1. Parameters of the particles used in the experiments.

450 mJ, pulse duration 10 ns). To create a spherical plasma, the laser beam is first expanded by a factor of 7.5 following the work of Xu *et al.* (2023). A convex lens with a 50 mm focal length then focuses the expanded beam, achieving convergence angle approximately 40°. To minimise the influence of the container walls on cavitation bubble behaviour, the distances between the focal point and the container walls are maintained at over 30 mm, significantly exceeding the maximum cavitation bubble radius ($R_{b,max} = 0.4-1.0$ mm).

Table 1 presents the range of the maximum cavitation bubble radius to particle radius ratio $R_{b,max}/R_p$. For PMMA particles with radius $R_p = 250$ μm, the ratio falls between 1.6 and 4.0. For PMMA particles with $R_p = 50$ μm, the ratio ranges from 8 to 20. Finally, for PS particles with $R_p = 25$ μm, the ratio lies within 16 and 40. The translation stage controls the vertical distance between the cavitation bubble and the wall, L, allowing for a dimensionless bubble stand-off distance $\gamma = L/R_{b,max}$ ranging from 1.0 to 5.0. With a smaller γ, the particle may contact the bottom interface of the laser-induced bubble during its growth and collapse, introducing the effects of surface tension and the bubble's internal pressure (Ren *et al.* 2022). To avoid this complexity, in this work, we focus on bubble–particle interactions without direct contact during the bubble's first cycle.

To achieve sufficient spatial and temporal resolution for observing particle interactions with cavitation bubbles of varying sizes, different combinations of high-speed cameras, lenses and light sources are employed. For PMMA particles with $R_p = 250$ μm, a high-speed camera (v711, Phantom) equipped with a macro lens (AF-S DX Micro-NIKKOR 40 mm f/2.8G, Nikon) captures images with spatial resolution 30.6 μm pixel^{-1}. A 150 W LED light source (FS-150, Nanguan) illuminates the high-speed images obtained at frame rate 2.1×10^5 frames per second (fps) with exposure time 4.4 μs. For both PMMA particles with $R_p = 50$ μm and PS particles with $R_p = 25$ μm, a high-speed camera (i-SPEED 726, iX Cameras) equipped with a body tube (1-50504, 12× UltraZoom, Navitar) and a long working distance microscope objective (M Plan Apo 10×, Mitutoyo) captures images with spatial resolution 2.4 μm pixel^{-1}. The high-speed camera operating at 1.0×10^5 fps with shutter speed 9.5 μs is illuminated by a pulsed laser illumination system (CAVILUX HF, CAVITAR, wavelength 810 nm, repetition rate 100 kHz, pulse duration 100 ns). All cameras and light sources are synchronised using a delay pulse signal generator (9524, Quantum Composers). The depth of field for both configurations confined the particles' front-to-back position within an error ± 40 μm, equivalent to ± 16 % of $R_{b,max}$. As noted previously, the translation stage controlled the particle's lateral position, ensuring a radial offset from the bubble's axis of symmetry within ± 20 % of $R_{b,max}$. This set-up guarantees that the particles are approximately located directly beneath the cavitation bubbles.

The position and radius of the cavitation bubble are measured from the high-speed snapshots with image processing techniques. The method varies depending on whether the entire bubble profile is fully captured within the field of view.

When the entire bubble is completely visualised within the image frame, the radius R_b^{full} is defined as the radius of a circle fitted to the entire bubble boundary using a least

https://doi.org/10.1017/jfm.2025.10998 Published online by Cambridge University Press

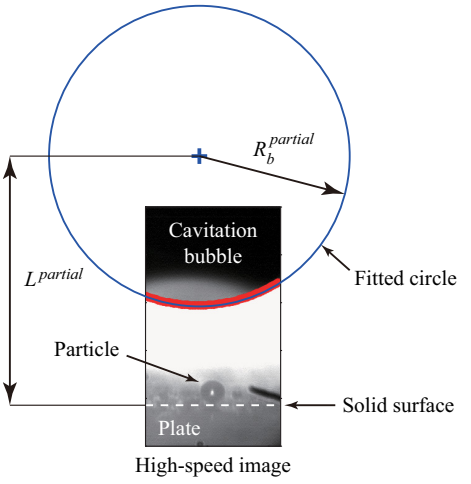


Figure 2. Boundary-fitting method to measure the position and radius of the cavitation bubble when the field of view is restricted. The superscript '*partial*' denotes bubble parameters obtained from this method.

squares minimisation algorithm implemented in a custom MATLAB (MathWorks) script (Ren *et al.* 2021). The superscript '*full*' indicates this full-boundary fitting method. The bubble position is correspondingly taken as the centre of this circle.

In cases where limitations of the field of view restrict the captured portion of the bubble, particularly for large bubble–particle radius ratios, a partial-boundary fitting method is employed. The contour line of the partially imaged cavitation bubble within the field of view (represented by the thick red line in figure 2) is fitted to a circle, as shown by the solid blue line, with the centre marked by a cross. The radius of the fitted circle is taken as the cavitation bubble radius $R_b^{partial}$, and the distance from the centre of the fitted circle to the solid surface is considered the distance $L^{partial}$ between the bubble centre and the wall, with the superscript '*partial*' denoting this partial-boundary fitting method.

As $\gamma^{partial} = L^{partial}/R_{b,max}^{partial}$ decreases (to approximately 1–1.5), the bubble's bottom flattens during its descent, leading to an overestimation of the maximum bubble radius (Ohl *et al.* 2006; Dijkink & Ohl 2008; Reuter, Zeng & Ohl 2022). The correlations between the same bubble parameters obtained from the two methods (e.g. $R_{b,max}^{full}$ and $R_{b,max}^{partial}$, γ^{full} and $\gamma^{partial}$) are established and detailed in Appendix A, which provides fitting functions to convert partial-boundary parameters to full-boundary ones. Unless otherwise specified, $R_{b,max}$ in the main text is reported with respect to the full-boundary fitting method, in which case the superscript '*full*' is omitted.

The particle centre position in each frame is also determined through circle fitting. Although the minimum spatial resolution is limited to 2.4 μm pixel^{-1}, the least squares minimisation algorithm constrains the vertical displacement measurement error to less than 0.6 pixels, in accordance with Ren *et al.* (2021, 2022).

2.2. *Numerical model*

To elucidate the mechanism by which γ and $R_{b,max}/R_p$ affect the particle's motion during the growth and collapse of the cavitation bubble, we perform numerical simulations within approximately axisymmetric computational domains, following the same geometrical relations as shown in figure 1. Since the particle size is much smaller than the bubble's maximum size, the particle's feedback on the flow field can be neglected, as supported by

https://doi.org/10.1017/jfm.2025.10998 Published online by Cambridge University Press

previous studies (Arora *et al.* 2004; Borkent *et al.* 2008; Wu *et al.* 2017, 2021). Thus our simulation adopts a one-way fluid–particle coupling scheme, in which the highly unsteady non-uniform flow field is simulated for a single cavitation bubble near a solid wall in the absence of the particle in OpenFOAM (Zeng *et al.* 2018*a*; Reuter *et al.* 2022), and the movement of the particle is subsequently predicted by integrating the hydrodynamic forces exerted by the fluid flow. In boundary layer flows, the one-way coupling approach has been validated for scenarios where the boundary layer thickness to particle radius ratio ranges between 0.1 and 10 (Vigolo *et al.* 2013, 2014). Furthermore, we note that implementing a two-way coupling scheme remains challenging for compressible three-phase flows in the current literature.

Here, we model the laser-induced cavitation bubble as a gas bubble in the framework of the finite volume method, which is a well-adapted method for simulating the first oscillating cycle (Koch *et al.* 2016). To capture the bubble dynamics, the volume fraction of the liquid phase α is defined. Considering mass conservation, the evolution of α is governed by the transport equation

$$\frac{\partial \alpha}{\partial t} + \nabla \cdot (\alpha \boldsymbol{U}) + \nabla \cdot (\alpha(1-\alpha)\boldsymbol{U_r}) = \alpha(1-\alpha)\left(\frac{\psi_g}{\rho_g} - \frac{\psi_l}{\rho_l}\right)\frac{\mathrm{D}p}{\mathrm{D}t} + \alpha\, \nabla \cdot \boldsymbol{U}, \tag{2.1}$$

where t is time, $\boldsymbol{U}$ is the flow velocity, ρ is the fluid density, and p is the flow pressure. Here, $\boldsymbol{U_r}$ is an artificial compressible term adjusting the sharpness of the interface (Rusche 2002). Flow compressibilities $\psi = \mathrm{D}\rho/\mathrm{D}p$ are modelled based on the equations of state for both gas and liquid. Subscripts g and l denote the gas and liquid phases, respectively.

Apart from the ultrashort nucleation and final collapse, the heat and mass transfer during the bubble expansion and shrinkage are negligible (Koch *et al.* 2016), therefore the flow is governed by the equations of continuity and momentum:

$$\frac{\partial \rho}{\partial t} + \nabla \cdot (\rho \boldsymbol{U}) = 0, \tag{2.2}$$

$$\frac{\partial \rho \boldsymbol{U}}{\partial t} + \nabla \cdot (\rho \boldsymbol{U}\boldsymbol{U}) = -\nabla p + \nabla \cdot \boldsymbol{\tau} + \boldsymbol{f}_\sigma, \tag{2.3}$$

where $\boldsymbol{\tau} = \mu[\nabla \boldsymbol{U} + \nabla \boldsymbol{U}^{\mathrm{T}} - (2/3)(\nabla \cdot \boldsymbol{U})\mathbf{I}]$ is the viscous stress tensor calculated based on the identity tensor $\mathbf{I}$ and the dynamic viscosity μ. The surface tension term $\boldsymbol{f}_\sigma$ is accounted for using the continuous surface force method (Brackbill, Kothe & Zemach 1992).

The simulated laser-induced bubble is initialised as a spherical gas pocket with a small radius and a high internal pressure. The gas follows a polytropic equation of state, while the liquid is considered as a compressible Tait liquid (Zeng *et al.* 2018*b*, 2024).

The schematic diagram in figure 3 presents the general set-up of the numerical simulations. The model is simplified to a two-dimensional axisymmetric configuration, with the computational domain defined as a 2° wedge. The domain extends to 20 $R_{b,max}$, and a structured mesh with progressive refinement from the outer region towards the inner region is applied. After eight successive refinements, the minimum grid spacing in both the bubble oscillation region and the vicinity of the wall reaches $\approx 0.0025\ R_{b,max}$, providing sufficient resolution in these critical zones. The symmetry plane is treated with wedge boundary conditions, the rigid wall is modelled as a no-slip boundary, and the remaining open boundaries are assigned wave-transmissive boundary conditions to suppress boundary effects. The ambient pressure is set to 101 315 Pa. To initialise the laser-induced bubble, a high-pressure spherical gaseous nucleus of radius $R_{b,0}$ is introduced

https://doi.org/10.1017/jfm.2025.10998 Published online by Cambridge University Press

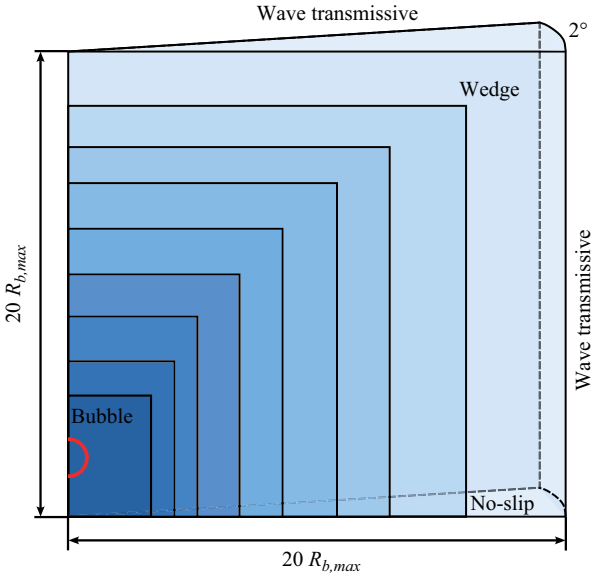


Figure 3. Numerical simulation set-up with progressive mesh refinement from coarse (light blue) to fine (dark blue).

into the flow field, with the initial pressure p_0 calibrated to reproduce the experimentally observed maximum radius and oscillation period.

Once the bubble oscillation is simulated, the resolved velocity and pressure fields are then applied to the force balance calculation of the particle. Assuming that the particle and the wall are both rigid, the particle is initially positioned on the wall directly below the cavitation bubble, with its centre at $(r = r_0, z = R_p)$. Here, r_0 denotes the initial radial offset in the simulation, which corresponds to the projected radial offset measured in the experiments. Given that $r_0 \ll R_{b,max}$, we focus our analysis on the particle's vertical motion.

For the motion of a spherical particle in the boundary flow induced by the cavitation bubble, we adopt the theories of the Basset–Boussinesq–Oseen equation (see Boussinesq 1885; Basset 1888; Oseen 1927; Annamalai & Balachandar 2017), the Maxey–Riley equation (see Maxey & Riley 1983), and the force expressions for the near-wall motion of a particle in a viscous stagnation flow (see Li *et al.* 2020). The forces on the particle include the viscous drag force $\boldsymbol{F}_{drag}$, the force induced by pressure gradient $\boldsymbol{F}_{pres}$, the added mass force $\boldsymbol{F}_{add}$, the net buoyancy force $\boldsymbol{F}_b$, and the wall-normal lubrication force $\boldsymbol{F}_{lub}$ (we neglect the Basset history force). The expressions for these forces are

$$\boldsymbol{F}_{drag} = \frac{1}{2} C_d \pi R_p^2 \rho_l \, \|\boldsymbol{U} - \boldsymbol{v}_p\| \big(\boldsymbol{U} - \boldsymbol{v}_p\big), \tag{2.4}$$

$$\boldsymbol{F}_{pres} = \oiint_{S_p} -p\boldsymbol{n}\mathrm{d}S = \iiint_{V_p} -\nabla p \mathrm{d}V, \tag{2.5}$$

$$\boldsymbol{F}_{add} = \frac{4}{3}\pi R_p^3 C_M \rho_l \left(\frac{\mathrm{D}\boldsymbol{U}}{\mathrm{D}t} - \frac{\mathrm{d}\boldsymbol{v}_p}{\mathrm{d}t} \right), \tag{2.6}$$

$$\boldsymbol{F}_b = \frac{4}{3}\pi R_p^3 \big(\rho_p - \rho_l\big)\boldsymbol{g}, \tag{2.7}$$

https://doi.org/10.1017/jfm.2025.10998 Published online by Cambridge University Press

$$\boldsymbol{F}_{lub} = -6\pi\mu_l R_p \frac{\boldsymbol{v}_p}{\epsilon}\left[1 - \frac{\epsilon}{5}\left(1 - \frac{1}{2}Re_v\right)\ln\epsilon\right]. \tag{2.8}$$

In these equations, $\boldsymbol{U}$ is the undisturbed flow velocity averaged over the particle volume, p is the undisturbed liquid pressure, $\boldsymbol{v}_p$ is the velocity of the particle centroid, S_p is the surface of the particle, V_p is the volume of the particle, $\boldsymbol{g}$ is the gravitational acceleration, C_d is the drag coefficient, C_M is the added mass coefficient ($C_M = 1/2$ for a sphere), ϵ is the dimensionless gap, and Re_v is a Reynolds number defined by $Re_v = \rho_l R_p v_p/\mu_l$ (Li *et al.* 2020).

The drag coefficient C_d is related to the particle Reynolds number Re_p given by

$$Re_p = \frac{\rho_l(2R_p)\,\|\boldsymbol{U} - \boldsymbol{v}_p\|}{\mu_l}. \tag{2.9}$$

In our problem, we estimate the characteristic magnitude of Re_p to be moderate ($Re_p \lesssim 250$, see Appendix C). Therefore, we adopt the empirical formula for C_d as a function of Re_p according to Clift, Grace & Weber (1978):

$$C_d = \frac{24}{Re_p}\left(1 + 0.15\,Re_p^{0.687}\right). \tag{2.10}$$

To prevent the divergence of the lubrication force F_{lub} as $\epsilon \to 0$, we model the gap as $\epsilon = (z_p + \Delta z_a)/R_p - 1$, similar to Vigolo *et al.* (2013). The parameter $\Delta z_a \approx 2$ nm is the lowest averaged roughness of the PMMA substrate, measured with a surface profiler (Zygo Nexview, USA). At particle–wall contact, a normal supporting force from the wall F_N is considered. The detachment criterion for the particle is defined as $F_N = 0$.

Applying Newton's second law of motion to the particle along the z-axis, we obtain

$$F_{drag} + F_{pres} + F_{add} + F_b + F_{lub} + F_N = F_h + F_N = \frac{4}{3}\pi R_p^3 \rho_p a_p, \tag{2.11}$$

where F_h is the resultant hydrodynamic force, and a_p is the vertical acceleration of the particle centroid. Solving (2.11) requires integration of the vertical particle velocity $v_p = \int_0^t a_p\,\mathrm{d}t$ and displacement $\Delta z = \int_0^t v_p\,\mathrm{d}t$.

The complete system of equations is implemented and solved numerically using MATLAB. The particle trajectory is computed by integrating the equations of motion using fixed time step 100 ns, which matches the temporal resolution of the flow field simulation. For computational implementation, several simplifications are introduced based on the flow characteristics. The undisturbed flow velocity $\boldsymbol{U}$ and pressure gradient force $\boldsymbol{F}_{pres}$ are calculated using volume averaging. Given the small particle size and minimal radial offset compared with the bubble maximum radius, the vertical undisturbed flow is approximately uniform within the particle's radial extent (as justified in Appendix B). Therefore, $\boldsymbol{U}$ is simplified to a line average from the particle bottom to top, treated as uniform on each radial cross-section of the particle. Similarly, the volume integral formulation of $\boldsymbol{F}_{pres}$ in (2.5) is employed for numerical computation, with the pressure gradient ∇p processed in the same manner as $\boldsymbol{U}$. Both $\boldsymbol{U}$ and ∇p are obtained by interpolating the flow field data at the particle position.

3. Results and discussion

3.1. *Experimental observations and comparison with simulation results*

We present the experimental and simulation results of the particle motion during the growth and collapse of the cavitation bubbles with four typical cases at various stand-off

https://doi.org/10.1017/jfm.2025.10998 Published online by Cambridge University Press

distances and size ratios. Figure 4 presents high-speed snapshots of cavitation bubble interaction with PMMA particles of radius $R_p = 250\,\mu\text{m}$ with comparable $R_{b,max}/R_p \approx 3.0$ and radial offset $r_0/R_p \approx 0.35$, but varying γ. The corresponding axisymmetric simulation results are superimposed. Note that the simulated particle profiles have been aligned horizontally with the experimental snapshots, while their vertical positions are unaltered. Here, red solid lines represent the positions of the solid surfaces, red dashed lines the bubble profiles, and dash-dotted lines the particle profiles in each frame.

Figure 4(*a*) shows results at $\gamma = 2.1$ and $R_{b,max}/R_p = 3.05$ for both the experiment and the simulation. In the high-speed snapshots, after the bubble is generated, it experiences an explosive growth with a spherical shape. A clearance is observed between the bottom of the particle and the plate before the bubble reaches its maximum radius (approximately 80.9 μs, see the enlarged view under frame (iv)). This behaviour is consistent with our observations in Ren *et al.* (2022). During bubble collapse (see frames (v)–(viii)), the particle exhibits a continuous upward motion. At the late stage of bubble collapse (158 μs), the bubble is no longer spherical, but it develops a micro-jet towards the boundary. Then the bubble evolves into a vortex ring, and its interactions with the particle have been reported in previous studies (Wu *et al.* 2021; Huang *et al.* 2024). Therefore, we only focus on the dynamics before the first collapse of the cavitation bubble. In the simulation results, figure 4(*a*), the profiles of the bubble and the particle fit well with the experiments, demonstrating the accuracy of our numerical model.

When we maintain the bubble-to-particle size ratio ($R_{b,max}/R_p = 3.06$), and increase the dimensionless stand-off distance γ to approximately 2.5 (see the snapshots in figure 4*b*), the bubble still shows a spherical shape during its explosive growth. The particle exhibits a finite but smaller vertical displacement before the bubble reaches its maximum radius (approximately 76.2 μs, see the enlarged view under frame (iv)). During bubble collapse (100 μs) and the late stage (152 μs), the particle upward displacement is reasonably smaller compared to figure 4(*a*), indicating that the bubble–particle interactions become weaker as γ becomes larger. Still, in this case, the profiles of the bubble and particle in the experimental and simulation results fit well, respectively.

Figures 5 and 6 present cavitation bubble interactions with PMMA particles of radius $R_p = 50\,\mu\text{m}$ under conditions with a radius ratio $R_{b,max}/R_p > 10$. In the high-speed snapshots, the cavitation bubble is partially shown in the upper portion of the images, with the position of the centroid and the radius obtained with the circle-fitting method as shown in figure 2. Using the conversion functions in Appendix A, the corresponding full-boundary parameters for the experimental cases are determined.

Figure 5 presents experimental observations for $\gamma = 1.3 \pm 0.2$, $R_{b,max}/R_p = 15 \pm 1$ and $r_0/R_p = 2.3$. From time zero to frame 8 (approximately 80 μs), the bubble's lower interface descends towards the solid boundary, indicating bubble growth. From frame 8 to frame 15, the lowest position of the interface remains, but the radius of curvature decreases, indicating bubble collapse. At frame 16 (160 μs), the bubble reaches the late collapse stage, exhibiting a dimple on top that develops into a micro-jet towards the surface. Particle displacement is visualised in the difference images shown beneath each snapshot, generated by subtracting each frame from a reference image before time zero. Bright areas in these images highlight the particle's displacement. Whilst minimal in frame 1, an upward and radially outward displacement is clearly visible by frame 2, as marked by the arrow. The particle continues to rise throughout the bubble's growth and collapse, reaching its maximum height (approximately 10 pixels, or 24 μm) at frame 16. Quantitative measurements are provided in figure 7. Since the particle has an original radial offset ($r_0 \approx 120\,\mu\text{m}$) with respect to the bubble's axis of symmetry, the particle moves outwards (frame 2–frame 7) and then inwards

https://doi.org/10.1017/jfm.2025.10998 Published online by Cambridge University Press

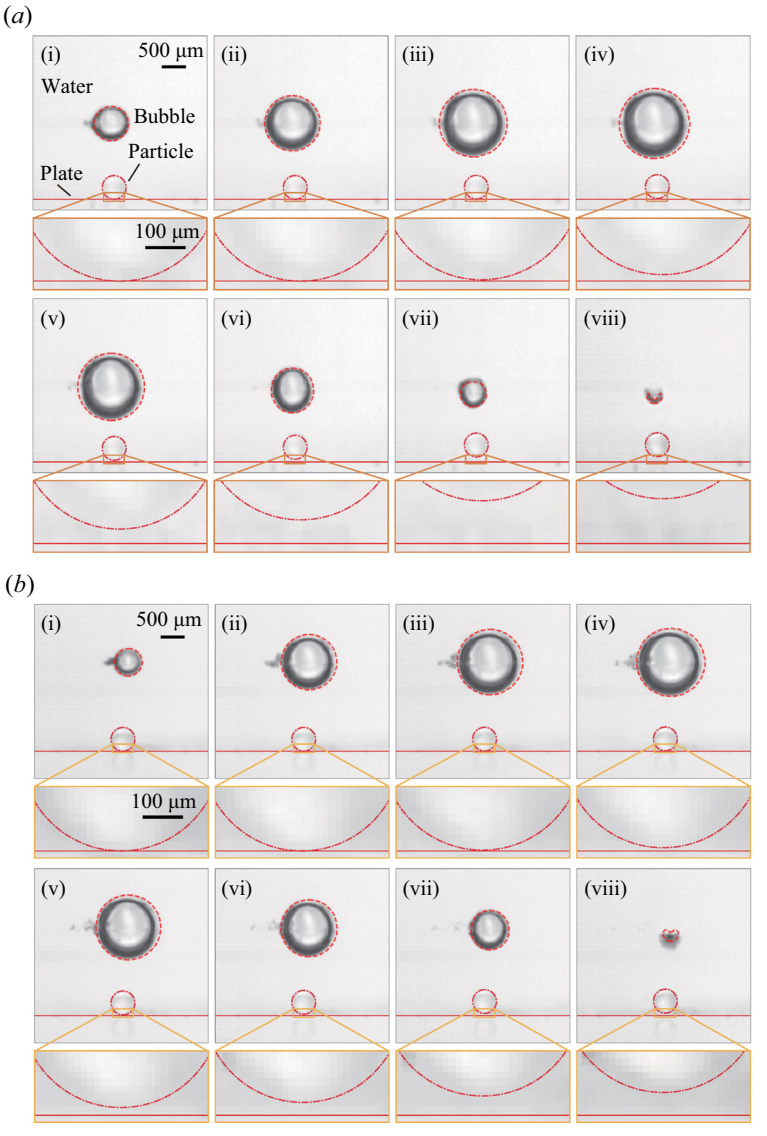


Figure 4. High-speed snapshots (grey-level images) and simulation results (red dashed and dash-dotted lines) of interactions between a cavitation bubble and a PMMA particle ($R_p = 250\,\mu$m). The experimental conditions for each case are: (*a*) $\gamma = 2.10 \pm 0.01$, $R_{b,max}/R_p = 3.05 \pm 0.01$, $r_0/R_p = 0.35$, and (*b*) $\gamma = 2.52 \pm 0.08$, $R_{b,max}/R_p = 3.06 \pm 0.01$, $r_0/R_p = 0.37$. The simulation is axisymmetric with parameters (*a*) $R_{b,0} = 35\,\mu$m, $p_0 = 970$ MPa, $\gamma = 2.10$, $R_{b,max}/R_p = 3.05$, and (*b*) $R_{b,0} = 35\,\mu$m, $p_0 = 884$ MPa, $\gamma = 2.50$, $R_{b,max}/R_p = 3.06$. The horizontal positions of the particle profiles in simulation have been aligned with the experimental snapshots for direct comparison, while the vertical dynamics are preserved. Time zero corresponds to the instant of laser plasma generation. In (*a*), the frame times for the snapshots are: (i) 9.52 μs, (ii) 28.6 μs, (iii) 57.2 μs, (iv) 80.9 μs, (v) 104 μs, (vi) 124 μs, (vii) 152 μs, and (viii) 158 μs. The frame times for the simulation results are: (i) 7.20 μs, (ii) 26.4 μs, (iii) 50.4 μs, (iv) 79.2 μs, (v) 103 μs, (vi) 122 μs, (vii) 151 μs, and (viii) 155 μs. In (*b*), the frame times for the snapshots are: (i) 4.76 μs, (ii) 28.6 μs, (iii) 52.4 μs, (iv) 76.2 μs, (v) 100 μs, (vi) 119 μs, (vii) 138 μs, and (viii) 152 μs. The frame times for the simulation results are: (i) 4.20 μs, (ii) 27.9 μs, (iii) 51.9 μs, (iv) 75.9 μs, (v) 99.9 μs, (vi) 119 μs, (vii) 138 μs, and (viii) 150 μs. For simulation results, the red solid lines represent the positions of the solid surfaces, the red dashed lines represent the bubble profiles, and the red dash-dotted lines represent the particle profiles in each frame. The regions focused on the bottom of the particle are enlarged and shown under each frame. See supplementary movie 1 for the experimental recordings at https://doi.org/10.1017/jfm.2025.10998.

https://doi.org/10.1017/jfm.2025.10998 Published online by Cambridge University Press

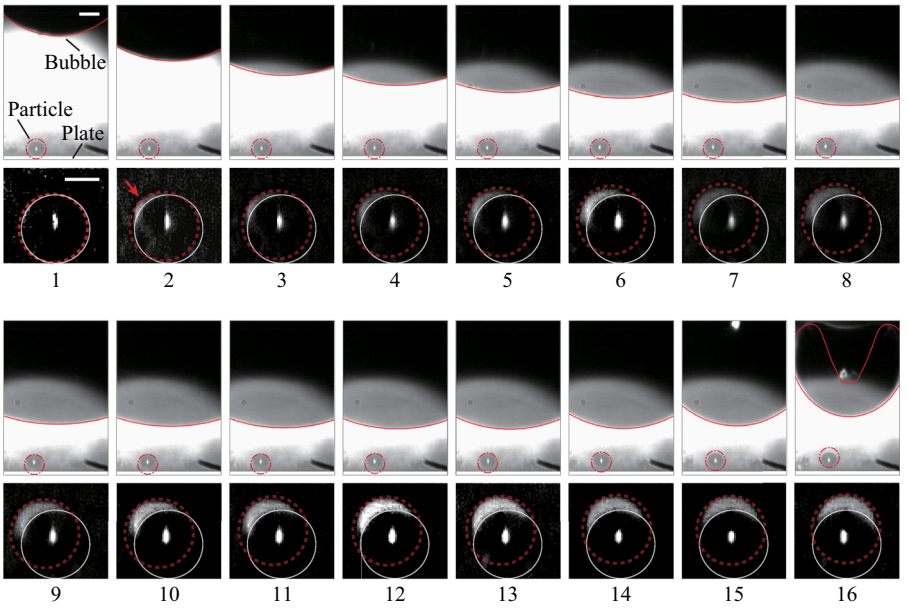


Figure 5. High-speed snapshots (grey-level images) and simulation results (red solid and dash-dotted lines) of interactions between a cavitation bubble and a PMMA particle ($R_p = 50\,\mu$m). The experimental condition is $\gamma = 1.3 \pm 0.2$, $R_{b,max}/R_p = 15 \pm 1$ and $r_0/R_p = 2.3$, where equivalent full-boundary parameters are used. The simulation condition is $R_{b,0} = 25\,\mu$m, $p_0 = 3600$ MPa, $\gamma = 1.3$, $R_{b,max}/R_p = 16$ and $r_0/R_p = 2.4$. The horizontal positions of the particle profiles in simulation have been aligned with the experimental snapshots for direct comparison, while the vertical dynamics are preserved. Time zero corresponds to the instant of laser plasma generation. The first frame (no. 1) for the snapshot is 10 μs, and for the simulation it is 8 μs. The time interval between frames is 10 μs, except for frame 16, where the time is 160 μs for the snapshot and 159 μs for the simulation. For simulation results, the red solid lines indicate the lower interface of the cavitation bubble, and the red dash-dotted lines represent the particle profiles in each frame. Beneath each snapshot, the difference image (reference frame before time zero minus current frame) highlights particle displacement (bright areas). The white solid line marks the particle's original position, and the red dotted line shows its profile at each time. In frame 2, the particle's initial vertical displacement becomes visible, as indicated by the arrow. Scale bars: 100 μm (main images), 50 μm (difference images). See supplementary movie 2 for the experimental recording.

(frame 8–frame 16), with a radial motion that appears to synchronise with the bubble's expansion and contraction. The particle's radial displacement is not the focus of this work. The original radial offset is intentionally minimised (see § 2.1), resulting in a negligible net radial displacement by the end of bubble collapse (frame 16). The simulated bubble profiles for $\gamma = 1.3$ and $R_{b,max}/R_p = 16$ demonstrate close agreement with the experimental observations throughout both the growth and collapse phases. The simulated particle profile ($r_0/R_p = 2.4$) also matches the experiment accurately from time zero until frame 15. A discrepancy arises in the late stage of bubble collapse (frame 16), where the simulation predicts a larger vertical displacement of the particle than observed experimentally. While an out-of-plane offset could potentially attenuate the vertical flow, Appendix B indicates that this factor plays only a limited role in influencing the particle vertical motion. The discrepancy is more likely attributed to the simplified force balance model, which may break down in the complex three-dimensional flow at the end of bubble collapse, potentially underestimating dissipative effects (Zeng *et al.* 2018*a*, 2022). This phenomenon requires further investigation. Nevertheless, the simulation successfully captures the primary features of the particle dynamics observed experimentally.

https://doi.org/10.1017/jfm.2025.10998 Published online by Cambridge University Press

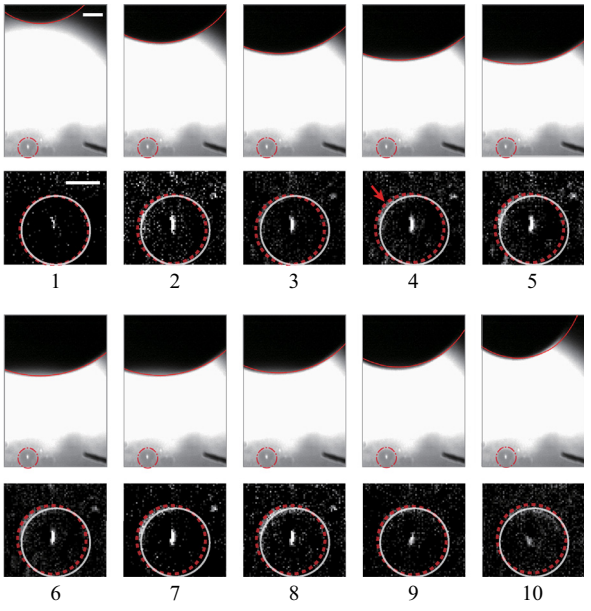


Figure 6. High-speed snapshots (grey-level images) and simulation results (red solid and dash-dotted lines) of interactions between a cavitation bubble and a PMMA particle ($R_p = 50\,\mu$m). The experimental condition is $\gamma = 1.8 \pm 0.1$, $R_{b,max}/R_p = 11 \pm 1$ and $r_0/R_p = 1.0$, where equivalent full-boundary parameters are used. The simulation condition is $R_{b,0} = 25\,\mu$m, $p_0 = 844$ MPa, $\gamma = 1.8$, $R_{b,max}/R_p = 11$ and $r_0/R_p = 1.0$. The horizontal positions of the particle profiles in simulation have been aligned with the experimental snapshots for direct comparison, while the vertical dynamics are preserved. Time zero corresponds to the instant of laser plasma generation. The first frame (no. 1) for the snapshot is 10 μs, and for the simulation it is 8.2 μs. The time interval between frames is 10 μs, except for frame 10 where the time is 100 μs for the snapshot and 96.4 μs for the simulation. For simulation results, the red solid lines indicate the lower interface of the cavitation bubble, and the red dash-dotted lines represent the particle profiles in each frame. Beneath each snapshot, the difference image (reference frame before time zero minus current frame) highlights particle displacement (bright areas). The white solid line marks the particle's original position, and the red dotted line shows its profile at each time. In frame 4, the particle's initial vertical displacement becomes visible, as indicated by the arrow. Scale bars: 100 μm (main images), 50 μm (difference images). See supplementary movie 2 for the experimental recording.

Figure 6 shows observations for $\gamma = 1.8$, $R_{b,max}/R_p = 11$ and $r_0/R_p = 1.0$. Similar to figure 5, the bubble lower interface descends towards the solid boundary from time zero to frame 5 (approximately 50 μs), indicating bubble growth. The bubble lower interface ascends away from the solid boundary from frame 6 to frame 10, showing an increase in the radius of curvature, indicating bubble collapse. The particle's vertical displacement becomes visualised as the thin, bright area to the upper left of its original position in the difference image at frame 4. This region is indicated by the arrow below the snapshot in figure 6. From frame 4 to frame 8, the particle rises slightly, as indicated by the expanding bright area in the difference image. Subsequently, at the end of bubble collapse (frames 9–10), this bright area diminishes slightly. Overall, the particle displacement in this case is less than 5 pixels ($\lesssim 12\,\mu$m), which is notably smaller than that observed in figure 5. Since the particle has a small initial radial offset ($r_0 \approx 50\,\mu$m) compared to the maximum bubble radius, the particle shows a minimal displacement in the radial direction until the end of bubble collapse. The simulation adopts $\gamma = 1.8$, $R_{b,max}/R_p = 11$ and $r_0/R_p = 1.0$. The simulated bubble profiles show good agreement with the experiments during growth and collapse. The simulation also captures the suppressed particle vertical displacement as observed.

https://doi.org/10.1017/jfm.2025.10998 Published online by Cambridge University Press

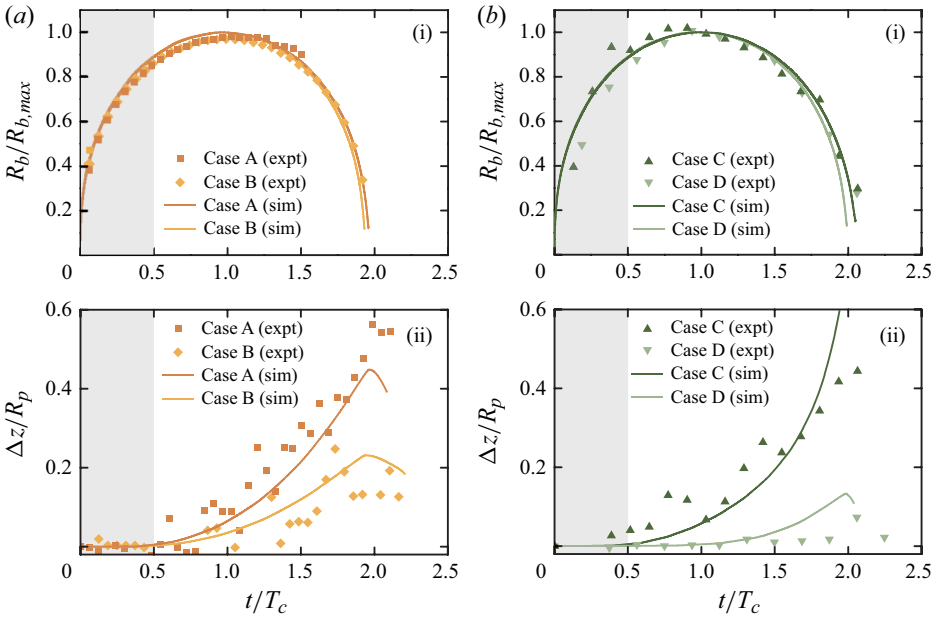


Figure 7. Evolution of the cavitation bubble radius and the particle displacement at different γ and $R_{b,max}/R_p$. (*a*) Results of PMMA particles with $R_p = 250\,\mu$m. Case A (expt): $\gamma = 2.10 \pm 0.01$, $R_{b,max}/R_p = 3.05 \pm 0.01$, $r_0/R_p = 0.35$. Case B (expt): $\gamma = 2.52 \pm 0.08$, $R_{b,max}/R_p = 3.06 \pm 0.01$, $r_0/R_p = 0.37$. Case A (sim): $\gamma = 2.1$, $R_{b,max}/R_p = 3.05$, $r_0/R_p = 0$. Case B (sim): $\gamma = 2.5$, $R_{b,max}/R_p = 3.06$, $r_0/R_p = 0$. (*b*) Results of PMMA particles with $R_p = 50\,\mu$m. For experiments, equivalent full-boundary parameters are used. Case C (expt): $\gamma = 1.3 \pm 0.2$, $R_{b,max}/R_p = 15 \pm 1$, $r_0/R_p = 2.3$. Case D (expt): $\gamma = 1.8 \pm 0.1$, $R_{b,max}/R_p = 11 \pm 1$, $r_0/R_p = 1.0$. Case C (sim): $\gamma = 1.3$, $R_{b,max}/R_p = 16$, $r_0/R_p = 2.4$. Case D (sim): $\gamma = 1.8$, $R_{b,max}/R_p = 11$, $r_0/R_p = 1.0$. In (*a*) and (*b*), panel (i) refers to the evolution of the dimensionless bubble radius $R_b/R_{b,max}$ with dimensionless time t/T_c with $T_c = R_{b,max}\sqrt{\rho_l/\Delta p}$, and panel (ii) refers to the evolution of the dimensionless vertical particle displacement $\Delta z/R_p$. The grey areas denote the period of bubble explosive growth.

Figure 7 shows the quantitative comparisons of the experimental and simulation results (cases A–D) in terms of the evolution of the cavitation bubble radius and the particle vertical displacement. The time is non-dimensionalised with the scale of bubble lifetime $T_c = R_{b,max}\sqrt{\rho_l/\Delta p}$ from the Rayleigh–Plesset equation (Rayleigh 1917; Plesset 1949), with $\Delta p = p_\infty - p_v$. Here, $p_\infty = 1.01 \times 10^5$ Pa is the ambient static pressure, and $p_v = 2.3 \times 10^3$ Pa is the vapour pressure at room temperature (Brennen 2014).

For cases A and B, the bubble radii of the simulation results $R_b/R_{b,max}$ agree well with the experiments, as shown in figure 7(*a*)(i). In figure 7(*a*)(ii), the particle's dimensionless displacement $\Delta z/R_p$ fits well between the experiments and the simulations. In both cases, the particle detaches from the substrate during the period of the bubble's explosive growth (before $t/T_c = 0.5$, see the grey area). From the decelerating growth of the bubble radius to the late stage before $t/T_c \approx 1.9$, the particle experiences an accelerating upward motion, then it decelerates and reaches the maximum height, and finally descends due to the jetting of the cavitation bubble (after collapse).

For cases C and D, the bubble radii of the simulation results $R_b/R_{b,max}$ show good agreement with the experimental values equivalent to the full-boundary fitting method; see figure 7(*b*)(i). The simulation results in figure 7(*b*)(ii) also align with experiments for case C, where the particle detaches from the substrate before $t/T_c = 0.5$, and exhibits accelerating upward motion during the bubble's first cycle with $\Delta z/R_p \lesssim 0.5$. In contrast,

https://doi.org/10.1017/jfm.2025.10998 Published online by Cambridge University Press

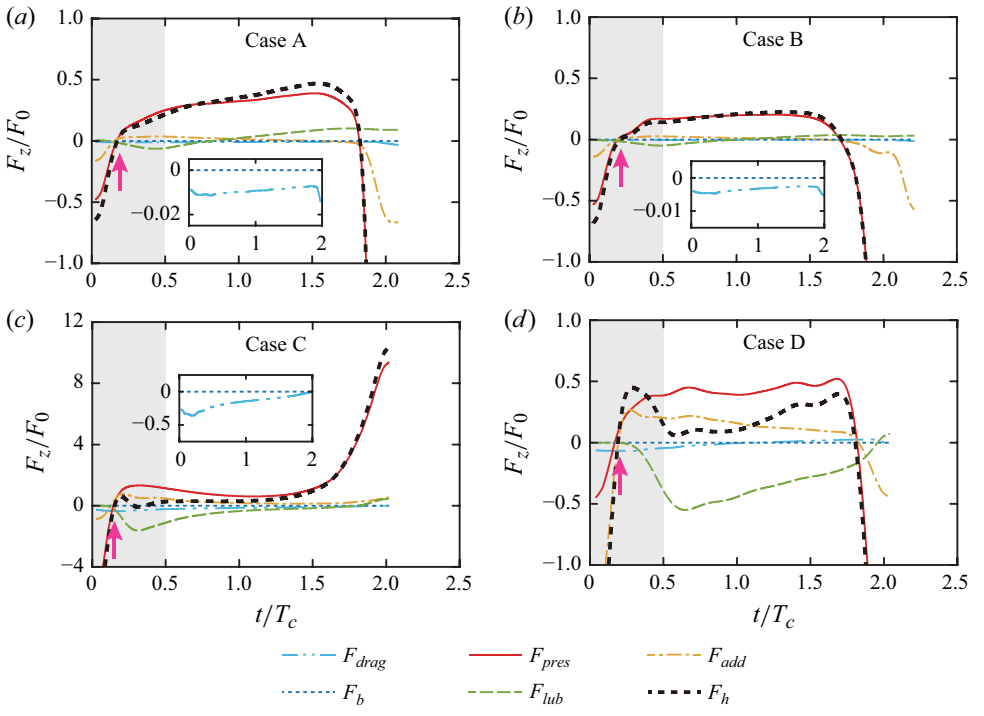


Figure 8. Evolution of the dimensionless hydrodynamic forces (smoothed) exerted on the PMMA particle in the vertical direction at different γ and $R_{b,max}/R_p$ with radii (*a*,*b*) $R_p = 250\,\mu$m and (*c*,*d*) $R_p = 50\,\mu$m. (*a*) Case A: $\gamma = 2.1$, $R_{b,max}/R_p = 3.05$, $r_0/R_p = 0$. (*b*) Case B: $\gamma = 2.5$, $R_{b,max}/R_p = 3.06$, $r_0/R_p = 0$. (*c*) Case C: $\gamma = 1.3$, $R_{b,max}/R_p = 16$, $r_0/R_p = 2.4$. (*d*) Case D: $\gamma = 1.8$, $R_{b,max}/R_p = 11$, $r_0/R_p = 1.0$. The characteristic scale for the force is $F_0 = m_p R_p/T_c^2$. The black dashed lines in (*a–d*) denote the resultant hydrodynamic force F_h. The arrows denote the instants at $F_h = 0$ during bubble explosive growth (period denoted by the grey areas). The insets in (*a–c*) are the enlarged views of F_{drag} and F_b.

for case D, the particle vertical displacement is strongly suppressed in the experiment, which is also captured by simulation ($\Delta z/R_p \lesssim 0.1$).

3.2. *Evolution of the hydrodynamic forces on the particle*

To understand the mechanisms behind the particle jump behaviours driven by cavitation bubbles, we show the evolution of the simulated forces on the particle, including the component forces from (2.4)–(2.8) and the resultant hydrodynamic forces, for cases A–D in figure 8. The forces are smoothed using a low-pass Butterworth filter, and non-dimensionalised by the characteristic force scale $F_0 = m_p R_p/T_c^2$, where m_p denotes the mass of the particle. In all cases, the resultant force F_h (thick black dashed line) converts its sign from negative (compressive force) to positive (lift force) during the bubble's explosive phase (within the grey area). Since the net buoyancy force F_b includes the weight of the particle, the instant for particle detachment is found at $F_h = 0$, as denoted by the arrows. Then the hydrodynamic force serves as a lift force until it decreases by the end of the bubble collapse, which is consistent with the cases for $R_{b,max}/R_p \sim 1$ as reported by Ren *et al.* (2022).

Dominant forces are identified by comparing the magnitudes of the component forces. For case A, the resultant force F_h is of the same magnitude as the pressure gradient force F_{pres} (red solid line) through the first cycle of bubble oscillation; see figure 8(*a*). The added

https://doi.org/10.1017/jfm.2025.10998 Published online by Cambridge University Press

mass force F_{add} (yellow dash-dotted line) shows the same sign conversion as F_{pres} but with an order of magnitude smaller than F_{pres}. The lubrication force F_{lub} (green dashed line) serves as a negative force after the particle detaches from the substrate (marked by the arrow), and converts its sign to positive at $t/T_c \approx 0.8$. Following the expression of F_{lub} in (2.8), this conversion corresponds to the sign of the term in the square bracket, with increasing gap thickness ϵ and increasing Reynolds number Re_v. During bubble growth, the magnitudes of $|F_{lub}|$ and $|F_{add}|$ are similar, and their contributions to the resultant hydrodynamic force balance each other. The viscous drag force F_{drag} (light blue dash-double-dotted line) remains negative, and its amplitude is only $\sim$20 % of $|F_{lub}|$. The net buoyancy force F_b (dark blue dotted line) remains a negative constant, and its absolute value is three orders of magnitude smaller than $|F_{drag}|$. For case B (figure 8*b*), the evolution of the component forces is similar to case A, although the magnitudes of the forces are reasonably smaller, about one-half of the magnitudes of the forces for case A.

For case C (figure 8*c*), the resultant force F_h is comparable in magnitude to the pressure gradient force F_{pres} during the bubble's explosive growth. After the particle detaches (marked by the arrow), the lubrication force F_{lub} serves as a resisting force with an amplitude similar to F_{pres}. This allows the added mass force F_{add} to become dominant until $t/T_c \approx 1.5$, after which F_{pres} regains dominance because F_{add} and F_{lub} eliminate each other. The viscous drag force $|F_{drag}|$ is one order of magnitude smaller than $|F_{lub}|$, while the net buoyancy force $|F_b|$ is three orders of magnitude smaller than $|F_{drag}|$. The significant difference in F_{pres} at the end of bubble collapse compared to cases A and B is caused by the distinct flow field and the boundary layer evolution, which will be discussed in § 3.3.

For case D, similar to case C, the added mass force F_{add} dominates during bubble growth, while F_{pres} and F_{lub} balance each other, as shown in figure 8(*d*). During bubble collapse, the lubrication force decreases and balances F_{add}, leading to the dominance of F_{pres}. Still, the viscous drag force $|F_{drag}|$ is one order of magnitude smaller than $|F_{lub}|$, while the net buoyancy force $|F_b|$ is three orders of magnitude smaller than $|F_{drag}|$.

In summary, the dominant force governing particle jump shifts with the bubble–particle size ratio. At small ratios ($R_{b,max}/R_p \sim 3$), the pressure gradient force F_{pres} dominates, while the added mass force F_{add} and the lubrication force F_{lub} balance each other. At large ratios ($R_{b,max}/R_p \gtrsim 10$), an enhanced lubrication force F_{lub} counteracts F_{pres}, allowing the added mass force F_{add} to dominate during bubble growth. This dynamic competition among F_{pres}, F_{add} and F_{lub} is the distinguishing feature of large size ratio cases. In all cases, the effects of F_{drag} and F_b are negligible.

3.3. *Evolution of the bubble-induced boundary layer flows*

To further understand how the evolution of the hydrodynamic forces on the particle is determined by the bubble-induced boundary layer flow, we look into the evolution of the flow velocity. Since we use the one-way fluid–particle coupling simulation, we show the simulation results of the undisturbed velocity distributions at $r = r_0$ between the bubble bottom and the substrate for different γ and $R_{b,max}/R_p$ (cases A–D); see figure 9. Panels (i) show U_z versus z/R_p, where the different line colours denote the dimensionless time t/T_c for each case.

Figure 9(*a*)(i) shows the typical evolution of the undisturbed velocity profiles between the bubble bottom and the solid wall for case A ($\gamma = 2.1$). At $t/T_c = 0.037$ (dark blue line), the negative velocity indicates a front stagnation flow towards the substrate at $\approx$ 1 m s^{-1} at level $z/R_p = 2$. As the bubble grows explosively, the fluid velocity (at the same level) increases ($t/T_c = 0.28$), indicating the accelerating growth of the bubble. Then the

https://doi.org/10.1017/jfm.2025.10998 Published online by Cambridge University Press

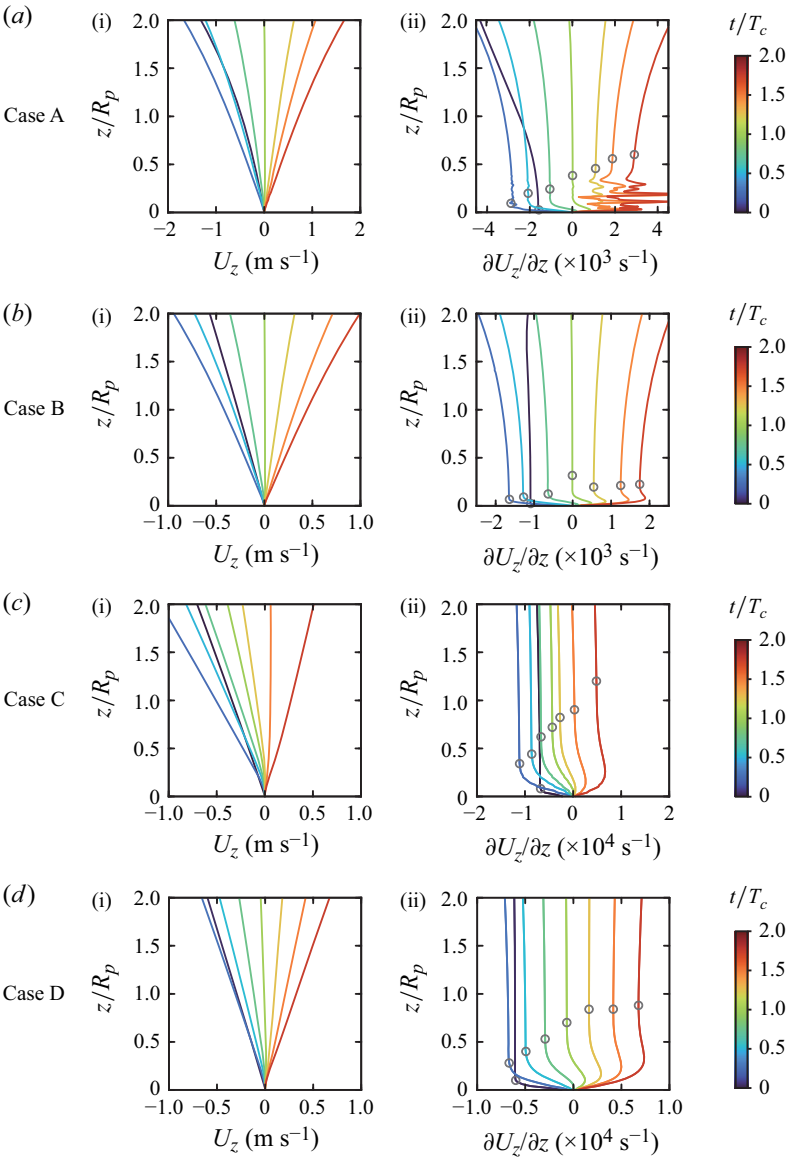


Figure 9. Simulation results of the undisturbed velocity distribution at $r = r_0$ with different γ and $R_{b,max}/R_p$ for PMMA particles with radii (*a*,*b*) $R_p = 250\,\mu$m and (*c*,*d*) $R_p = 50\,\mu$m. (*a*) Case A: $\gamma = 2.1$, $R_{b,max}/R_p = 3.05$, $r_0/R_p = 0$. (*b*) Case B: $\gamma = 2.5$, $R_{b,max}/R_p = 3.06$, $r_0/R_p = 0$. (*c*) Case C: $\gamma = 1.3$, $R_{b,max}/R_p = 16$, $r_0/R_p = 2.4$. (*d*) Case D: $\gamma = 1.8$, $R_{b,max}/R_p = 11$, $r_0/R_p = 1.0$. In (*a–d*), panel (i) refers to the profile of the wall-normal velocity U_z, and panel (ii) refers to the vertical velocity gradient $\partial\, U_z/\partial\, z$. The colour bar on the right denotes the dimensionless time t/T_c for each case. The grey circles in panel (ii) indicate the boundary layer thickness δ/R_p at the different times. In (*a*), the times t/T_c are 0.037, 0.28, 0.52, 0.76, 1.00, 1.24, 1.48 and 1.72; in (*b*), the times t/T_c are 0.025, 0.27, 0.51, 0.75, 0.99, 1.23, 1.47 and 1.71; in (*c*), the times t/T_c are 0.013, 0.26, 0.51, 0.75, 1.00, 1.25, 1.49 and 1.74; in (*d*), the times t/T_c are 0.045, 0.29, 0.53, 0.77, 1.02, 1.26, 1.50 and 1.74.

https://doi.org/10.1017/jfm.2025.10998 Published online by Cambridge University Press

bubble growth decelerates ($t/T_c = 0.28$–1.00) until the bubble grows to its maximum size when the velocity becomes approximately zero. During the bubble's collapse, the velocity becomes positive and increases again, indicating a rear stagnation flow ($t/T_c = 1.00$–1.72). Compared with case A, the velocity profiles are similar for case B ($\gamma = 2.5$, see figure 9*b*i) and case D ($\gamma = 1.8$, see figure 9*d*i), indicating that the evolution of the flow field between the bubble bottom and the rigid wall is similar. For case C ($\gamma = 1.3$, see figure 9*c*i), which is a particular representative for a bubble with flat bottom during growth and collapse, the bubble's explosive growth phase can be obviously observed before $t/T_c = 0.26$. Yet before $t/T_c = 1.49$ (orange line), the velocity remains negative, indicating that the front stagnation flow lasts until the late stage of the bubble collapse.

Then we analyse the evolution of the boundary layer thickness for the different cases based on the velocity profiles. From the solution to the axisymmetric stagnation (Homann) flow (Homann 1936), we know that the potential flow solution out of the boundary layer is $U_z = -2Bz$ and $U_r = Br$, where B is the strain rate of the flow, z is the vertical distance from the wall, and r is the radial distance from the axis. Within the boundary layer, the component velocities read $U_z = -2B\ f(z)$ and $U_r = Br\ \mathrm{d}f/\mathrm{d}z$, where $f(z)$ is a function determining the velocity profile. Outside the boundary layer, $z \gg \delta$, the function $f(z)$ fulfils $f(z) \to z$ and $\mathrm{d}f/\mathrm{d}z \to 1$. The boundary layer thickness δ is defined as the normal distance from the wall where the radial velocity component is equal to 99 % of the corresponding free-stream value, i.e. $(\mathrm{d}f/\mathrm{d}z)|_{(z=\delta)} = 0.99$. We prove in § 3.4 that with $r, z \ll L$, $R_{b,max}$ the analytical solution to the bubble-induced stagnation flow has the same form as the Homann solution. Based on this, we identify the boundary layer thickness δ by finding the position where the vertical velocity gradient $\partial\, U_z/\partial\, z$ reaches 99 % of a constant value. As shown in panels (ii) of figure 9, the boundary layer thickness δ/R_p for each case is denoted by the grey circles at the selected times.

The evolution of the unsteady boundary layer thickness with time (δ/R_p versus t/T_c) is plotted in figure 10, which is superimposed with the central position of the particle, $z_p/R_p = 1 + \Delta z/R_p$, for comparisons. For case A (figure 10*a*), the boundary layer thickness δ/R_p increases slowly from zero to approximately 0.25 at $t/T_c \approx 1.0$. Then the boundary layer grows fast to a peak value $\delta/R_p \approx 0.9$ (close to the particle centre) at $t/T_c \approx 1.1$ as the bubble reaches its maximum size (see figure 7*a*i). As the bubble collapses, the boundary layer thickness decreases and approaches a constant $\delta/R_p \approx 0.5$ until $t/T_c = 1.95$. The boundary layer thickness remains less than 50 % of the particle radius during most time of the bubble's oscillation, indicating that the particle is mainly subjected to the force induced by the inviscid flow field, corresponding to the leading role of the pressure gradient force F_{pres}.

For case B (figure 10*b*), the evolution of the boundary layer thickness during bubble growth is similar to case A, with a smaller peak value ($\delta/R_p \approx 0.4$) at the bubble's maximum size ($t/T_c \approx 1.0$). During bubble collapse, the boundary layer thickness remains a constant $\delta/R_p \approx 0.2$, less than that of case A. The evolution of δ/R_p also indicates that the particle's motion is dominated by the inviscid flow field.

For case C (figure 10*c*), the boundary layer thickness increases from zero to a peak value $\delta/R_p \approx 1.8$ at $t/T_c \approx 1.8$, exceeding the position of the particle centre. Then it drops to $\delta/R_p \approx 1$ by the end of bubble collapse. The peak of the boundary layer thickness is delayed because the front stagnation flow is largely retarded due to the lasting downward motion of the bubble bottom, as already seen in figure 5. During this time period, the particle motion is largely influenced by the boundary layer flow, leading to a large lubrication force F_{lub}. After $t/T_c \approx 1.8$, the particle centre is suddenly exposed to the outer flow again, causing an abrupt increase in F_{pres} as observed in figure 8(*c*).

https://doi.org/10.1017/jfm.2025.10998 Published online by Cambridge University Press

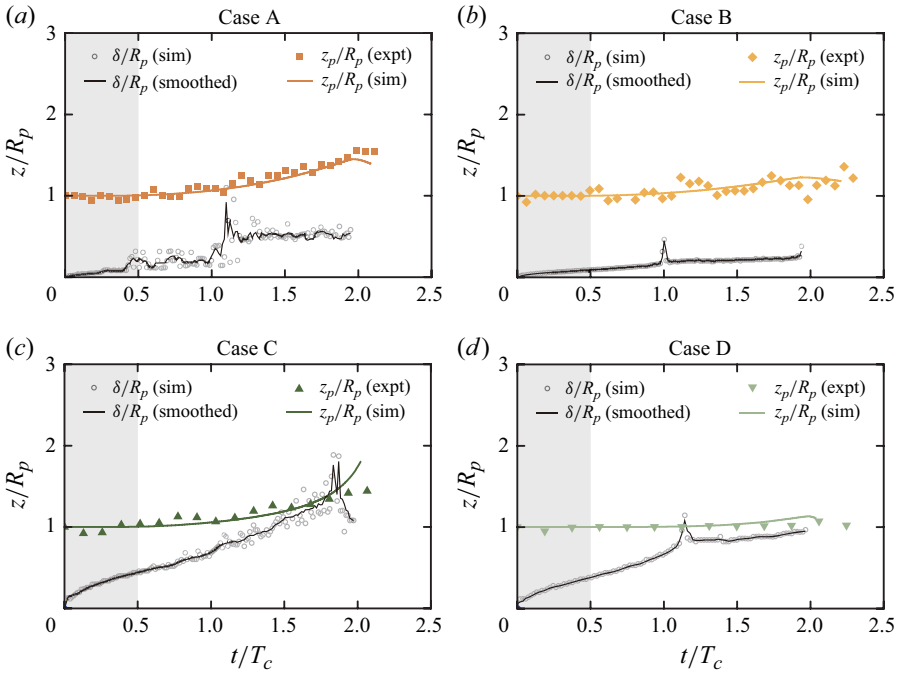


Figure 10. Simulation results of evolution of the dimensionless boundary layer thickness δ/R_p at $r = r_0$ with different γ and $R_{b,max}/R_p$ for PMMA particles with radii (*a*,*b*) $R_p = 250\,\mu$m and (*c*,*d*) $R_p = 50\,\mu$m. (*a*) Case A: $\gamma = 2.1$, $R_{b,max}/R_p = 3.05$, $r_0/R_p = 0$. (*b*) Case B: $\gamma = 2.5$, $R_{b,max}/R_p = 3.06$, $r_0/R_p = 0$. (*c*) Case C: $\gamma = 1.3$, $R_{b,max}/R_p = 16$, $r_0/R_p = 2.4$. (*d*) Case D: $\gamma = 1.8$, $R_{b,max}/R_p = 11$, $r_0/R_p = 1.0$. The boundary layer thickness δ/R_p is compared with the position of the particle centre z_p/R_p in each case. For the experimental data, bubble parameters obtained from the partial-boundary fitting method are converted into their full-boundary equivalents. The grey areas in (*a–d*) denote the period of bubble explosive growth.

For case D (figure 10*d*), the boundary layer thickness δ/R_p grows fast from zero to a peak value of approximately 1.0 at $t/T_c \approx 1.1$, then it maintains at the level 0.9 until the end of bubble collapse, almost immersing the particle centre. During bubble growth, compared with cases A and B, the front stagnation flow in case D is retarded near the particle centre, allowing the fast increase of the lubrication force F_{lub} shown in figure 8(*d*), which suppresses the particle vertical motion.

3.4. *Scaling analysis of the particle displacement at the end of bubble collapse*

To elucidate the scaling law for the particle's displacement at the end of bubble collapse, we perform a model analysis of the dynamics of the cavitation bubble–particle interaction. Figure 11 presents a schematic of the model for the flow fields induced by a cavitation bubble without particles. In figure 11(*a*), we assume an axisymmetric stagnation point flow between the bubble's bottom interface and the rigid wall. This flow includes a viscous boundary layer with a time-dependent thickness δ, reflecting the unsteady nature of the cavitation bubble dynamics. The velocity components within the boundary layer ($z < \delta$) are denoted by (u_r, u_z), while the velocity components outside the boundary layer are (U_r, U_z). For simplification, the velocity field outside the boundary layer is assumed to be approximately equivalent to the solution obtained from the potential flow model, as shown in figure 11(*b*). Following the potential flow theory framework established in Best & Blake (1994), the flow field induced by the cavitation bubble is superimposed with its

https://doi.org/10.1017/jfm.2025.10998 Published online by Cambridge University Press

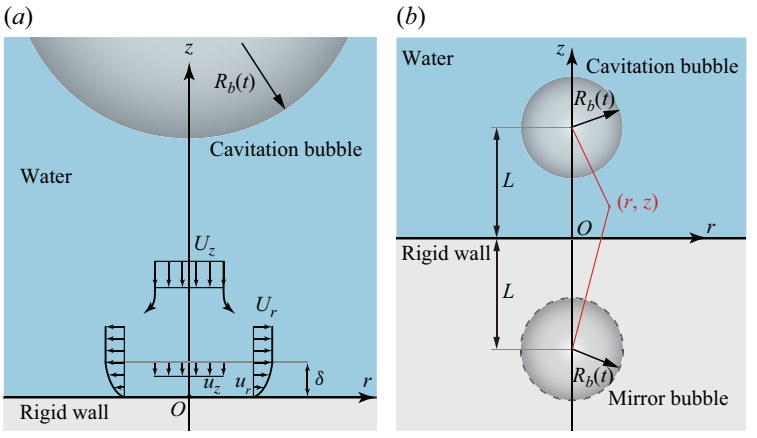


Figure 11. Schematic of the theoretical model for cavitation bubble-induced flow near a rigid boundary. (*a*) The flow field near the stagnation point under a growing cavitation bubble. (*b*) The flow field outside the boundary layer established by a spherical cavitation bubble near a solid wall with the method of images.

mirror image symmetric about a horizontal rigid wall. This approach satisfies the boundary condition of zero normal velocity at the rigid wall.

In cylindrical coordinates, the flow field is symmetric about the z-axis passing through the centre of the cavitation bubble. Consistent with prior works (Best & Blake 1994; Wu *et al.* 2021; Ren *et al.* 2022), the cavitation bubble is modelled as a sphere with a time-dependent radius $R_b(t)$. A point source of strength $Q(t) = 4\pi R_b^2 \dot{R}_b$ is placed at the bubble's centre, where $\dot{R}_b$ represents the velocity at the bubble interface. A second, identical point source is positioned at the location of the mirror image cavitation bubble, symmetric about the plane $z = 0$. The flow velocity $\boldsymbol{U} = (U_r, U_z)$ at any point (r, z) with an arbitrary rotation angle about the z-axis is the superposition of the velocities induced by both point sources:

$$U_r = R_b^2 \dot{R}_b \left\{ \frac{r}{\left[r^2 + (L-z)^2\right]^{3/2}} + \frac{r}{\left[r^2 + (L+z)^2\right]^{3/2}} \right\}, \tag{3.1}$$

$$U_z = R_b^2 \dot{R}_b \left\{ \frac{-(L-z)}{\left[r^2 + (L-z)^2\right]^{3/2}} + \frac{L+z}{\left[r^2 + (L+z)^2\right]^{3/2}} \right\}. \tag{3.2}$$

The time evolution of the cavitation bubble radius is governed by the modified Rayleigh equation near the solid wall (Best & Blake 1994):

$$R_b \ddot{R}_b + \frac{3}{2}\dot{R}_b^2 + \frac{R_b}{2L}\left(R_b \ddot{R}_b + 2\dot{R}_b^2\right) = -\frac{\Delta p}{\rho_l}, \tag{3.3}$$

where $\ddot{R}_b$ denotes the acceleration of the bubble interface, with the driving pressure difference $\Delta p = p_\infty - p_v$, where $p_\infty = 1.01 \times 10^5$ Pa is the pressure in the far field, and $p_v = 2.3 \times 10^3$ Pa is the vapour saturation pressure. The initial conditions for (3.3) are $R_b(0) = R_{b,max}$ and $\dot{R}_b(0) = 0$. Solving (3.3) yields $R_b(t)$, which describes the collapse of a cavitation bubble from its maximum radius. To obtain the complete $R_b(t)$ curve encompassing both growth and collapse phases, the solution curve is reflected about the time point where $R_b = R_{b,max}$ and the time zero is shifted to the instant of bubble generation (Obreschkow, Bruderer & Farhat 2012; Wu *et al.* 2017).

https://doi.org/10.1017/jfm.2025.10998 Published online by Cambridge University Press

Within the region close to the bottom of the cavitation bubble ($r, z \ll L$, $R_{b,max}$), the potential flow field described by (3.1) and (3.2) can be further simplified:

$$\begin{cases} U_r = \dfrac{2R_b^2\dot{R}_b}{L^3}\, r, \\ U_z = -\dfrac{4R_b^2\dot{R}_b}{L^3}\, z. \end{cases} \tag{3.4}$$

Here, we define $B = 2R_b^2\dot{R}_b/L^3$ with units s^{-1}. With this substitution, (3.4) becomes

$$\begin{cases} U_r = Br, \\ U_z = -2Bz. \end{cases} \tag{3.5}$$

The simplified inviscid flow field solution in (3.5) resembles the outer flow field of the steady axisymmetric stagnation flow solution presented by Homann (1936). However, our case involves a highly unsteady flow where B varies with time due to the cavitation bubble's growth and collapse.

Following a method similar to that of Homann (1936), the Navier–Stokes equations governing viscous flow are established. Substituting the inviscid solution (3.5) into the Euler equations in cylindrical coordinates:

$$\begin{cases} \dfrac{\partial U_r}{\partial t} + U_r\dfrac{\partial U_r}{\partial r} + U_z\dfrac{\partial U_r}{\partial z} = -\dfrac{1}{\rho_l}\dfrac{\partial p}{\partial r}, \\ \dfrac{\partial U_z}{\partial t} + U_r\dfrac{\partial U_z}{\partial r} + U_z\dfrac{\partial U_z}{\partial z} = -\dfrac{1}{\rho_l}\dfrac{\partial p}{\partial z}. \end{cases} \tag{3.6}$$

After simplification, the equations governing the inviscid pressure field are obtained:

$$\begin{cases} \dfrac{\partial p}{\partial r} = -\rho_l\big(\dot{B} + B^2\big)r, \\ \dfrac{\partial p}{\partial z} = -\rho_l\big(-2\dot{B} + 4B^2\big)z, \end{cases} \tag{3.7}$$

with $\dot{B} = \mathrm{d}B/\mathrm{d}t$. Integrating (3.7) and introducing the stagnation pressure p_{st} yields

$$p = p_{st} - \frac{1}{2}\rho_l\big[\big(\dot{B} + B^2\big)r^2 + \big(-2\dot{B} + 4B^2\big)z^2\big]. \tag{3.8}$$

The viscous flow solution is assumed to be

$$\begin{cases} u_r = Br\dfrac{\mathrm{d}f}{\mathrm{d}z}, \\ u_z = -2B\, f(z). \end{cases} \tag{3.9}$$

Here, $f(z)$ is an undetermined function of spatial coordinate z. The pressure field of the viscous flow solution is also assumed to be

$$p = p_{st} - \frac{1}{2}\rho_l\big[\big(\dot{B} + B^2\big)r^2 + \big(-2\dot{B} + 4B^2\big)\, g(z)\big], \tag{3.10}$$

where $g(z)$ is an undetermined function. We then substitute the viscous flow solution from (3.9) into the continuity equation and Navier–Stokes equations in cylindrical coordinates:

https://doi.org/10.1017/jfm.2025.10998 Published online by Cambridge University Press

$$\begin{cases} \dfrac{\partial u_r}{\partial r}+\dfrac{u_r}{r}+\dfrac{\partial u_z}{\partial z}=0, \\ \dfrac{\partial u_r}{\partial t}+u_r\dfrac{\partial u_r}{\partial r}+u_z\dfrac{\partial u_r}{\partial z}=-\dfrac{1}{\rho_l}\dfrac{\partial p}{\partial r}+\nu_l\left(\dfrac{\partial^2 u_r}{\partial r^2}+\dfrac{1}{r}\dfrac{u_r}{r}-\dfrac{u_r}{r^2}+\dfrac{\partial^2 u_r}{\partial z^2}\right), \\ \dfrac{\partial u_z}{\partial t}+u_r\dfrac{\partial u_z}{\partial r}+u_z\dfrac{\partial u_z}{\partial z}=-\dfrac{1}{\rho_l}\dfrac{\partial p}{\partial z}+\nu_l\left(\dfrac{\partial^2 u_z}{\partial r^2}+\dfrac{1}{r}\dfrac{u_z}{r}+\dfrac{\partial^2 u_z}{\partial z^2}\right), \end{cases} \tag{3.11}$$

where ν_l is the kinematic viscosity of water. The continuity equation is automatically satisfied. Below, we simplify the Navier–Stokes equation in the r-direction.

In the following derivation, $\mathrm{d}f/\mathrm{d}z$ is abbreviated as f', $\mathrm{d}^2 f/\mathrm{d}z^2$ as f'', and $\mathrm{d}^3 f/\mathrm{d}z^3$ as f'''. The simplified Navier–Stokes equation in the r-direction becomes

$$f'''+\frac{2B}{\nu_l}ff''+\frac{B}{\nu_l}\left(1-f'^2\right)+\frac{\dot{B}}{\nu_l B}\left(1-f'\right)=0. \tag{3.12}$$

This equation governs the axisymmetric viscous stagnation flow induced by the cavitation bubble.

The boundary conditions for (3.12) at time t are given by

$$\begin{cases} z=0, & f'(0)=f(0)=0, \\ z\to\infty, & f'(z)\to 1. \end{cases} \tag{3.13}$$

The no-slip boundary condition ($f=f'=0$) applies at the solid wall ($z=0$). The far-field boundary condition indicates that the velocity profile approaches the inviscid flow ($f'=1$) as the distance from the wall z increases far beyond the boundary layer thickness.

The time-dependent nature of parameter B in (3.12) presents a significant challenge for obtaining a numerical solution. As noted by Kolomenskiy & Moffatt (2012), solutions to similar unsteady viscous stagnation flow equations are highly sensitive to the parameter $\dot{B}/B^2$. Depending on the range of $\dot{B}/B^2$, the equation may exhibit various solution behaviours, including single-valued, bifurcated, multi-valued, or even no solution at all. These complexities likely reflect instabilities within the boundary layer of the actual flow.

Therefore, a detailed analysis of solving (3.12) and the characteristics of its solutions is deferred for future work. Instead, we leverage a simplified form of (3.12) to identify key parameters and derive scaling laws for particle motion.

To link the flow field to the displacement of the particle, we leverage the momentum theorem. The particle's velocity $v_{p,end}$ at the end of bubble collapse T_{end} (before jet penetration) reads

$$v_{p,end}=\frac{\int_0^{T_{end}}F_z\,\mathrm{d}t}{m_p}, \tag{3.14}$$

where F_z ($=F_h+F_N$) represents the vertical force acting on the particle. We denote the time of particle detachment from the solid surface as t_0. Since the vertical force acting on the particle remains zero ($F_z=0$) before t_0, the integral in (3.14) reduces to

$$\int_0^{T_{end}}F_z\,\mathrm{d}t=\int_{t_0}^{T_{end}}F_z\,\mathrm{d}t. \tag{3.15}$$

After particle detachment ($\Delta z>0$), from figure 8 we find that the resultant force on the particle equals F_h, which is dominated by the sum of the pressure gradient force F_{pres}, the added mass force F_{add}, and the lubrication force F_{lub}. Here, we estimate the lower and

https://doi.org/10.1017/jfm.2025.10998 Published online by Cambridge University Press

upper bounds of the integral (3.15) as

$$\int_{t_0}^{T_{end}} F_{add}\,\mathrm{d}t \lesssim \int_{t_0}^{T_{end}} F_z\,\mathrm{d}t \lesssim \int_{t_0}^{T_{end}} F_{pres}\,\mathrm{d}t. \tag{3.16}$$

From the Navier–Stokes equation, the pressure gradient force (2.5) is related to the fluid unsteady inertia as

$$\boldsymbol{F}_{pres} = \iiint_{V_p} -\nabla p \mathrm{d}V \approx \iiint_{V_p} \rho_l \frac{\mathrm{D}\boldsymbol{u}}{\mathrm{D}t}\mathrm{d}V, \tag{3.17}$$

where $\boldsymbol{u}$ is the undisturbed fluid velocity in the stagnation flow field. In (3.17), the viscous terms are omitted for the limited contribution of the viscous drag force. This expression is equivalent to the undisturbed force in Annamalai & Balachandar (2017). By simplifying the right-hand side of (3.17) with the undisturbed fluid velocity at the particle centre ($z = z_p$), we obtain

$$F_{pres} \approx \frac{4}{3}\pi R_p^3 \rho_l \left.\frac{\mathrm{D}u_z}{\mathrm{D}t}\right|_{(z=z_p)}. \tag{3.18}$$

The added mass force is linked to the pressure gradient force as $F_{add} \approx (1/2)F_{pres} - (1/2)(\rho_l/\rho_p)F_z$.

From (3.14)–(3.18), we obtain

$$\begin{aligned} v_{p,end} &\lesssim \frac{\rho_l}{\rho_p}\left[u_z\big(z=z_p, t=T_{end}\big) - u_z\big(z=z_p, t=t_0\big)\right], \\ v_{p,end} &\gtrsim \frac{\rho_l}{2\rho_p+\rho_l}\left[u_z\big(z=z_p, t=T_{end}\big) - u_z\big(z=z_p, t=t_0\big)\right]. \end{aligned} \tag{3.19}$$

Recalling (3.9), we recognise that at the end of the bubble collapse ($R_b \to 0$), the parameter $B(T_{end})$ approaches zero. Thus we can infer $u_z(z=z_p, t=T_{end}) \to 0$. From the evolution of the particle's displacement with time (figure 7), we approximate the particle's velocity at the end of bubble collapse $v_{p,end}$ as twice the average velocity $\Delta z_{end}/\Delta T$, with $\Delta T = T_{end} - t_0$.

To solve for the right-hand side of (3.19), we now need to derive the flow velocity $u_z(z=z_p, t=t_0)$ at the centre of the particle at time $t=t_0$ when the particle is about to leave the substrate ($z_p = R_p$). By comparing the position of the particle centre and the boundary layer thickness, we consider two regimes: (i) when the particle centre is far beyond the boundary layer at t_0, i.e. $\delta(t_0)/R_p \ll 1$, the particle detachment is dominated by the inviscid flow; and (ii) when the particle centre position is comparable to or lower than the boundary layer thickness at t_0, i.e. $\delta(t_0)/R_p \gtrsim 1$, the particle detachment is dominated by the viscous flow. In regime (i), we recall (3.5) and have

$$u_z\big(z=R_p, t=t_0\big) = -2B(t_0)\,R_p \quad \text{for } \delta(t_0)/R_p \ll 1. \tag{3.20}$$

In regime (ii), we recall (3.9) and have

$$u_z\big(z=R_p, t=t_0\big) = -2B(t_0)\,f(R_p) \quad \text{for } \delta(t_0)/R_p \gtrsim 1. \tag{3.21}$$

To estimate the vertical liquid velocity $u_z(z=R_p, t=t_0)$ for both regimes, we need to approximate the value of $B(t_0)$.

For regime (i) with $\delta(t_0)/R_p \ll 1$, from figures 8(*a*) and 8(*b*) we find that at $t=t_0$, the hydrodynamic force F_h is dominated by the pressure gradient force, thus with $F_{pres} = 0$. Substituting (3.18) into $F_{pres}(t_0) = 0$ yields solving $\mathrm{D}u_z/\mathrm{D}t = 0$ at $t = t_0$.

https://doi.org/10.1017/jfm.2025.10998 Published online by Cambridge University Press

For regime (ii) with $\delta(t_0)/R_p \gtrsim 1$, from figures 8(*c*) and 8(*d*) we find that at $t = t_0$, the hydrodynamic force F_h is dominated by the added mass force, thus with $F_{add} = 0$. Substituting (2.6) and $a_p(t_0) = \mathrm{d}v_p/\mathrm{d}t = 0$ into $F_{add}(t_0) = 0$ also yields solving $\mathrm{D}u_z/\mathrm{D}t = 0$ at $t = t_0$.

We now focus on regime (ii). Substituting (3.9) into $\mathrm{D}u_z/\mathrm{D}t = 0$ at $z = R_p$ and $t = t_0$, we obtain

$$\left(\dot{B} f - 2B^2 f f'\right)\Big|_{(z=R_p,\ t=t_0)} = 0. \tag{3.22}$$

Since both $f(R_p)$ and $B(t_0)$ are non-zero, solving (3.22) for t_0 reduces to solving $\dot{B}/(2B^2) = f'(R_p)$.

When the particle centre position is comparable to the boundary layer thickness at t_0, i.e. $\delta(t_0)/R_p \sim 1$, we assume $f'(R_p) \approx 1$. This leads to

$$\left(R_b^2 \ddot{R}_b + 2R_b \dot{R}_b^2 - \frac{4}{L^3} R_b^4 \dot{R}_b^2\right)\Big|_{(t=t_0)} = 0. \tag{3.23}$$

Eliminating $\ddot{R}_b$ in (3.3) by using (3.23), we express the bubble wall velocity at $t = t_0$ as

$$\dot{R}_b|_{(t=t_0)} = \sqrt{\frac{\Delta p}{\rho_l}\left[-\frac{2}{\gamma^4}\left(\frac{R_b}{R_{b,max}}\right)^4 - \frac{4}{\gamma^3}\left(\frac{R_b}{R_{b,max}}\right)^3 + \frac{1}{2}\right]^{-1}}\Bigg|_{(t=t_0)}. \tag{3.24}$$

To further eliminate $\dot{R}_b$, we can leverage the solution provided by Best & Blake (1994) for the modified Rayleigh equation for a growing cavitation bubble near a solid wall:

$$\dot{R}_b\sqrt{\frac{\rho_l}{\Delta p}} = \sqrt{\frac{2}{3}\left(1 + \frac{1}{2\gamma}\frac{R_b}{R_{b,max}}\right)^{-1}\left[\left(\frac{R_{b,max}}{R_b}\right)^3 - 1\right]}. \tag{3.25}$$

Combining (3.24) and (3.25), we obtain

$$\left[\frac{4}{\gamma^4}\left(\frac{R_b}{R_{b,max}}\right)^7 + \frac{8}{\gamma^3}\left(\frac{R_b}{R_{b,max}}\right)^6 - \left(\frac{3}{2\gamma} + \frac{4}{\gamma^4}\right)\left(\frac{R_b}{R_{b,max}}\right)^4 - \left(4 + \frac{8}{\gamma^3}\right)\left(\frac{R_b}{R_{b,max}}\right)^3 + 1\right]\Bigg|_{(t=t_0)} = 0. \tag{3.26}$$

The solution to (3.26) depends on the dimensionless stand-off distance γ. Numerical calculations show that for the range of γ considered in this work (1.0–5.0), the solution $(R_b/R_{b,max})|_{(t=t_0)}$ falls within the range (0.419, 0.618), and the non-dimensional time t_0/T_c ranges from 0.0608 to 0.159, both increasing with increasing γ. Then the value of $B(t_0)$ can be calculated through

$$B(t_0) = \frac{2}{\gamma^3} G(\gamma)\sqrt{\frac{\Delta p}{\rho_l}} R_{b,max}^{-1}, \tag{3.27}$$

with a function

$$G(\gamma) = \frac{\left(R_b/R_{b,max}\right)|^2_{(t=t_0)}}{\sqrt{-\frac{2}{\gamma^4}\left(\frac{R_b}{R_{b,max}}\right)\Big|^4_{(t=t_0)} - \frac{4}{\gamma^3}\left(\frac{R_b}{R_{b,max}}\right)\Big|^3_{(t=t_0)} + \frac{1}{2}}}. \tag{3.28}$$

https://doi.org/10.1017/jfm.2025.10998 Published online by Cambridge University Press

The function $G(\gamma)$ increases with increasing γ, and its value ranges between 0.463 and 0.544 with $\gamma \in (1.0, 5.0)$. Therefore, within this range, we can approximate $G(\gamma)$ as a constant, i.e. $G(\gamma) \approx 0.5$. Consequently, the value of $B(t_0)$ is approximated as

$$B(t_0) \approx \frac{1}{\gamma^3}\sqrt{\frac{\Delta p}{\rho_l}}\, R_{b,max}^{-1} = \gamma^{-3}\, T_c^{-1}. \tag{3.29}$$

When the particle centre is far below the edge of the boundary layer at t_0, i.e. $\delta(t_0)/R_p \gg 1$, we assume $f'(R_p) \to 0$. This leads to

$$\left(2R_b\dot{R}_b^2 + R_b^2\ddot{R}_b\right)\Big|_{(t=t_0)} = 0. \tag{3.30}$$

Following a similar procedure from (3.24) to (3.29) (for details see Appendix D), we arrive at

$$B(t_0) \approx \gamma^{-3} T_c^{-1}. \tag{3.31}$$

The result above coincides with (3.29) for $f'(R_p) \to 1$.

To estimate the undisturbed liquid velocity $u_z(z = R_p, t = t_0)$ for $\delta(t_0)/R_p \gtrsim 1$, we can simplify the solution to (3.12) by approximating $f'''(z)$ as a linear function, i.e. $f'''(z) \approx -f'''(0)(z/\delta_0 - 1)$, where $\delta(t_0)$ is denoted as δ_0 for simplification. By integration while combining the boundary conditions ($f'(0) = f(0) = 0$) and $f'(\delta_0) = 0.99$, we obtain

$$\begin{aligned}
f(z) &\approx 0.2475\delta_0\left(\frac{z}{\delta_0} - 1\right)^4 + 0.99z - 0.2475\delta_0,\\
f'(z) &\approx 0.99\left(\frac{z}{\delta_0} - 1\right)^3 + 0.99,\\
f''(z) &\approx \frac{2.97}{\delta_0}\left(\frac{z}{\delta_0} - 1\right)^2,\\
f'''(z) &\approx \frac{5.94}{\delta_0^2}\left(\frac{z}{\delta_0} - 1\right),
\end{aligned} \tag{3.32}$$

with $f'''(0) \approx -5.94/\delta_0^2$ under the condition $0 \leqslant z \leqslant \delta_0$. Therefore, $f(R_p)$ is a function of R_p and δ_0. To determine δ_0, from (3.12) and (3.22), we notice $f'''(0) = -(B(t_0)/\nu_l) - [\dot{B}(t_0)/(\nu_l B(t_0))] = -(B(t_0)/\nu_l)[1 + 2\, f'(R_p)]$. Combining this relation with $f'(R_p) \approx 0.99(R_p/\delta_0 - 1)^3 + 0.99$ and the expression for $B(t_0)$ (both (3.29) and (3.31) give the same result), we derive an equation for δ_0/R_p:

$$\left(\frac{\delta_0}{R_p}\right)^3 + 5.94\left(\frac{\delta_0}{R_p}\right)^2 - 5.94\left[1 + \gamma^3\left(\frac{R_{b,max}}{R_p}\right)^2 Re_b^{-1}\right]\left(\frac{\delta_0}{R_p}\right) + 1.98 = 0, \tag{3.33}$$

with the bubble Reynolds number based on the maximum bubble radius

$$Re_b = \frac{R_{b,max}\sqrt{\Delta p/\rho_l}}{\nu_l}. \tag{3.34}$$

The solution to (3.33) can be evaluated by numerical calculation.

https://doi.org/10.1017/jfm.2025.10998 Published online by Cambridge University Press

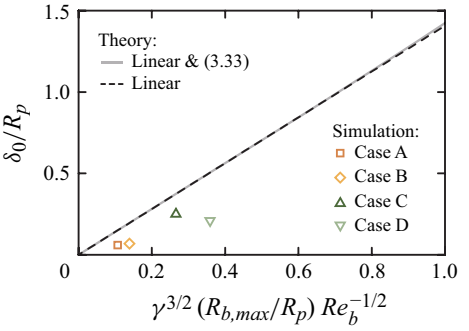


Figure 12. Boundary layer thickness at particle detachment (δ_0/R_p) as a function of the stand-off distance γ, the bubble–particle radius ratio $R_{b,max}/R_p$, and the bubble Reynolds number Re_b. The solid grey line denotes the combination of the linear solution (3.35) and the numerical solution to (3.33). The dashed black line denotes the linear relationship only. The data points denote δ_0/R_p in simulations (cases A–D) read from figure 10.

For $\delta_0/R_p \ll 1$, we have $f'(R_p) = 1$, and then $f'''(0) = -3\,B(t_0)/\nu_l \approx -5.94/\delta_0^2$, leading to $\delta_0 \approx \sqrt{1.98\nu_l/B(t_0)}$, or

$$\frac{\delta_0}{R_p} \approx 1.41\gamma^{3/2}\left(\frac{R_{b,max}}{R_p}\right) Re_b^{-1/2}. \tag{3.35}$$

The solutions shown in figure 12 indicate that the linear relationship (3.35) holds approximately for the range of δ_0/R_p from 0 to 1.5. In figure 12, δ_0/R_p from the simulation results (figure 10) shows a similar trend to the lines, validating the above theoretical derivations.

Finally, to simplify (3.19), we write the non-dimensionalised forms of (3.20) and (3.21), and combine them as

$$\frac{u_z(z = R_p, t = t_0)}{\sqrt{\Delta p/\rho_l}} \approx -2\gamma^{-3}\left(\frac{R_{b,max}}{R_p}\right)^{-1}\mathcal{F}, \tag{3.36}$$

with a function

$$\mathcal{F} = \begin{cases} 1 & \text{for } \delta_0/R_p \ll 1, \\ \dfrac{f(R_p)}{R_p} & \text{for } \delta_0/R_p \gtrsim 1. \end{cases} \tag{3.37}$$

From figure 12, we identify $\mathcal{F}$ as a function of $\gamma^{3/2}(R_{b,max}/R_p)\,Re_b^{-1/2}$. Therefore, we arrive at

$$\begin{aligned} \frac{v_{p,end}}{\sqrt{\Delta p/\rho_l}} &\lesssim 2\frac{\rho_l}{\rho_p}\gamma^{-3}\left(\frac{R_{b,max}}{R_p}\right)^{-1}\mathcal{F}, \\ \frac{v_{p,end}}{\sqrt{\Delta p/\rho_l}} &\gtrsim \frac{2\rho_l}{2\rho_p + \rho_l}\gamma^{-3}\left(\frac{R_{b,max}}{R_p}\right)^{-1}\mathcal{F}. \end{aligned} \tag{3.38}$$

Then we simplify the relationship $v_{p,end} \sim 2\,\Delta z_{end}/\Delta T$ by approximating T_{end}/T_c as $1.83(1 + 0.205/\gamma)$ (Rattray 1951; Reuter *et al.* 2022). For the range of γ considered in our work (1.0–5.0), and recalling the range of t_0/T_c, the ratio $\Delta T/T_c = (T_{end} - t_0)/T_c$ is approximately equal to 2. Then we have

https://doi.org/10.1017/jfm.2025.10998 Published online by Cambridge University Press

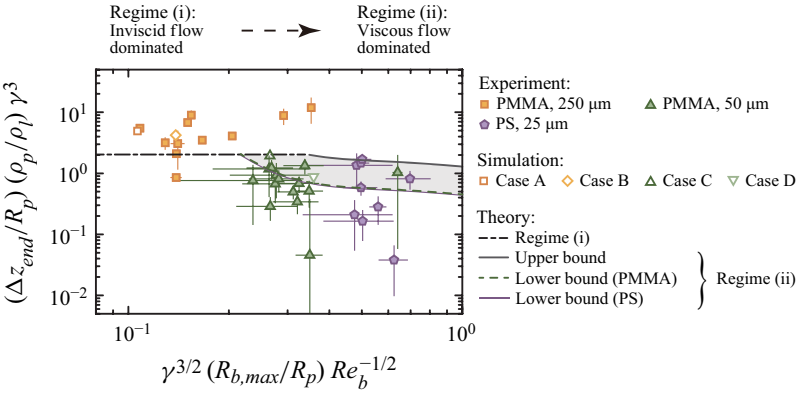


Figure 13. Relationship between $(\Delta z_{end}/R_p)\,(\rho_p/\rho_l)\,\gamma^3$ and $\gamma^{3/2}(R_{b,max}/R_p)\,Re_b^{-1/2}$. Data points for experiments are differentiated by markers representing the type and radius of the particles, and the simulation results (cases A–D) are presented, as shown in the legend. The shaded region in regime (ii) represents (3.39) with the upper and lower bounds for different particle densities. For the experimental data, bubble parameters obtained from the partial-boundary fitting method are converted into their full-boundary equivalents.

$$\frac{2\rho_l}{2\rho_p+\rho_l}\gamma^{-3}\mathcal{F} \lesssim \frac{\Delta z_{end}}{R_p} \lesssim 2\frac{\rho_l}{\rho_p}\gamma^{-3}\,\mathcal{F}. \tag{3.39}$$

Based on this, figure 13 shows the relationship between $(\Delta z_{end}/R_p)\,(\rho_p/\rho_l)\,\gamma^3$ and $\gamma^{3/2}(R_{b,max}/R_p)\,Re_b^{-1/2}$, with the results of experiments and simulations. When $\gamma^{3/2}(R_{b,max}/R_p)\,Re_b^{-1/2}$ is below ~ 0.2, the inviscid flow dominates the particle motion (regime (i), corresponding to $\delta_0/R_p \ll 1$), leading to $\Delta z_{end}/R_p(\rho_p/\rho_l)\gamma^3 \sim 2$ (dash-dotted black line). This regime is supported by the experimental cases of PMMA particles with $R_p = 250\,\mu$m and the simulation cases A and B. When $\gamma^{3/2}(R_{b,max}/R_p)\,Re_b^{-1/2}$ exceeds ~ 0.2 (corresponding to a larger boundary layer thickness comparable to R_p), the dominating mechanism for particle motion transfers to regime (ii), leading to the decrease of $(\Delta z_{end}/R_p)\,(\rho_p/\rho_l)\,\gamma^3$ with the increase of $\gamma^{3/2}(R_{b,max}/R_p)\,Re_b^{-1/2}$, as supported by the experimental cases of PMMA particles with $R_p = 50\,\mu$m, and PS particles with $R_p = 25\,\mu$m, as well as the simulation cases C and D. The two lower bounds of the shaded region (regime (ii)) arise from the different density ratios ρ_l/ρ_p, but the two curves almost overlap each other for the small density differences between PMMA and PS.

It is important to clarify the limitations of the theoretical analysis in this work. The assumptions made here, namely that the particle has negligible influence on the flow field around the cavitation bubble, and that the flow field coordinates (r, z) at the particle's location satisfy $r, z \ll L, R_{b,max}$, may not hold for the cases with $R_{b,max}/R_p \lesssim 1$ or bubble–particle contact. In such scenarios, the pressure distribution on the particle surface should be considered, and the particle's motion may be dominated by the net pressure difference caused by the vapour pressure inside the bubble during contact, which has been described by Ren *et al.* (2022).

4. Conclusions

This study combines experiments, simulations and theoretical analysis to investigate how boundary layer flows influence cavitation bubble-driven particle detachment from

https://doi.org/10.1017/jfm.2025.10998 Published online by Cambridge University Press

a rigid wall. Experiments with laser-induced cavitation bubbles and particles of varying densities and radii demonstrate the universality of particle detachment during bubble growth across a wide range of radius ratios ($1.6 \leqslant R_{b,max}/R_p \leqslant 40$) and bubble stand-off distances ($1.0 \leqslant \gamma \leqslant 5.0$). Surprisingly, increasing $R_{b,max}/R_p$ at fixed γ suppresses particle displacement during the bubble's first cycle of growth and collapse.

To elucidate the underlying mechanisms, we employ a one-way fluid–particle coupling simulation, modelling the bubble dynamics while neglecting feedback from the particle. The simulations, validated against experiments, reveal that the dominant forces on the particle shift with $R_{b,max}/R_p$ at fixed γ. For small size ratios, the pressure gradient force dominates throughout the bubble's lifetime, whereas for large ratios, the added mass force dominates before transitioning to the pressure gradient force due to the influence of the lubrication force. The competition among the forces is linked to the boundary layer development in the bubble-induced stagnation flows. The boundary layer thickness remains below $0.5R_p$ for small $R_{b,max}/R_p$, but approaches R_p for large ratios, suppressing particle vertical motion.

A theoretical framework, combining the potential flow theory (Best & Blake 1994) and an axisymmetric viscous stagnation flow model (Homann 1936), provides scaling laws for particle displacement. By comparing the particle's position with the boundary layer thickness at detachment, we identify two regimes: (i) an inviscid flow dominated regime, where particle motion is governed by potential flows, and (ii) a viscous flow dominated regime, where boundary layer effects prevail. The derived scaling laws align with experimental and numerical results.

This work advances the understanding of unsteady boundary layer effects in cavitation-driven particle motion near rigid walls. The findings offer theoretical insights for applications such as microparticle manipulation, particle removal, cavitation erosion, and flow visualisation techniques such as particle image velocimetry.

Supplementary movies. Supplementary movies are available at https://doi.org/10.1017/jfm.2025.10998.

Acknowledgements. We gratefully acknowledge Professor H.A. Stone and Professor C. Sun for helpful discussions.

Funding. This work was supported by the National Natural Science Foundation of China (nos 12402297, U24A20140, 52076120, 52079066 and 12302313), the Postdoctoral Fellowship Programme of China Postdoctoral Science Foundation (nos GZB20240336 and 2025M771853), and the Shuimu Tsinghua Scholar Programme (no. 2023SM227).

Declaration of interests. The authors report no conflict of interest.

Appendix A. Relationship between the bubble parameters obtained from the full- and partial-boundary fitting methods

To infer parameters under full boundary conditions from those obtained from the partial-boundary fitting method, we conduct experiments on a single cavitation bubble near a solid wall, as illustrated in figure 14(*a*). The bubble is fully visible in the high-speed video, and its radius is determined using the full-boundary fitting method as R_b^{full}, with the fitted circle shown as a thin red line in figure 14(*a*).

To establish relationships between parameters derived from the two methods, we simulate conditions in which only the bottom portion of the bubble is visible by cropping the image using a window of width w, aligned with the bubble's axis of symmetry. From the partial boundary (thick red line), the radius is fitted as $R_b^{partial}$, represented by the

https://doi.org/10.1017/jfm.2025.10998 Published online by Cambridge University Press

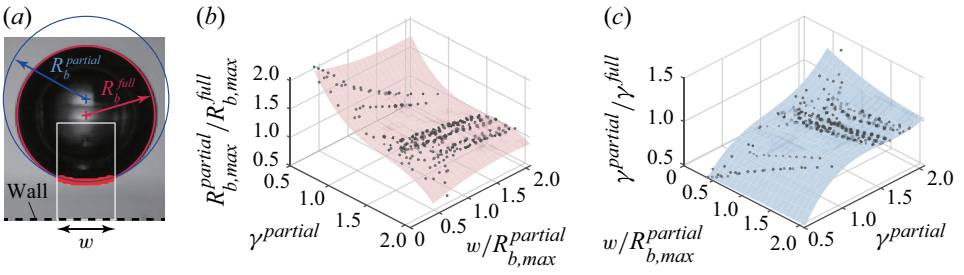


Figure 14. Relationship between bubble parameters obtained from the full- and partial-boundary fitting methods. (*a*) Measurement of parameters from a high-speed snapshot of a single cavitation bubble near a solid wall using both methods. The fitted circle from the full-boundary method is shown as a thin red line, while that from the partial-boundary method is shown as a thin blue line. The white box indicates the fitting window of width w for the partial boundary (thick red line). (*b*) Relationship between $R_{b,max}^{partial}/R_{b,max}^{full}$ and $(\gamma^{partial}, w/R_{b,max}^{partial})$. (*c*) Relationship between $\gamma^{partial}/\gamma^{full}$ and $(\gamma^{partial}, w/R_{b,max}^{partial})$. In (*b*) and (*c*), solid dots represent experimental measurements, and curved surfaces show polynomial fits, with their mathematical expressions given in (A1) and (A2).

circle in a thin blue line. The dimensionless stand-off distance is also obtained from both methods as $\gamma^{partial}$ and γ^{full}.

Then we systematically vary the window size and stand-off distance, obtaining a series of measured data in dimensionless form as $(\gamma^{partial}, w/R_{b,max}^{partial})$. The relationship between $R_{b,max}^{partial}/R_{b,max}^{full}$ and $(\gamma^{partial}, w/R_{b,max}^{partial})$ is shown in figure 14(*b*), while the relationship between $\gamma^{partial}/\gamma^{full}$ and $(\gamma^{partial}, w/R_{b,max}^{partial})$ is presented in figure 14(*c*). Experimental data are represented as solid dots.

Polynomial functions with interaction terms are fitted to the experimental data, as illustrated by the curved surfaces. The fitted functions take the following forms:

$$\begin{aligned}\frac{R_{b,max}^{partial}}{R_{b,max}^{full}} = {} & 4.155 - 5.561\,\gamma^{partial} - 0.6611\,\frac{w}{R_{b,max}^{partial}} + 3.611\,\left(\gamma^{partial}\right)^2 \\ & + 0.3512\,\gamma^{partial}\,\frac{w}{R_{b,max}^{partial}} + 0.2046\,\left(\frac{w}{R_{b,max}^{partial}}\right)^2 - 0.8511\,\left(\gamma^{partial}\right)^3 \\ & + 0.08012\,\left(\gamma^{partial}\right)^2\,\frac{w}{R_{b,max}^{partial}} - 0.1586\,\gamma^{partial}\,\left(\frac{w}{R_{b,max}^{partial}}\right)^2, \end{aligned} \tag{A1}$$

$$\begin{aligned}\frac{\gamma^{partial}}{\gamma^{full}} = {} & -0.4206 + 2.568\,\gamma^{partial} - 0.06239\,\frac{w}{R_{b,max}^{partial}} - 1.856\,\left(\gamma^{partial}\right)^2 \\ & + 0.3104\,\gamma^{partial}\,\frac{w}{R_{b,max}^{partial}} - 0.04335\,\left(\frac{w}{R_{b,max}^{partial}}\right)^2 + 0.5022\,\left(\gamma^{partial}\right)^3 \\ & - \left(\gamma^{partial}\right)^2\,\frac{w}{R_{b,max}^{partial}} + 0.06028\,\gamma^{partial}\,\left(\frac{w}{R_{b,max}^{partial}}\right)^2. \end{aligned} \tag{A2}$$

https://doi.org/10.1017/jfm.2025.10998 Published online by Cambridge University Press

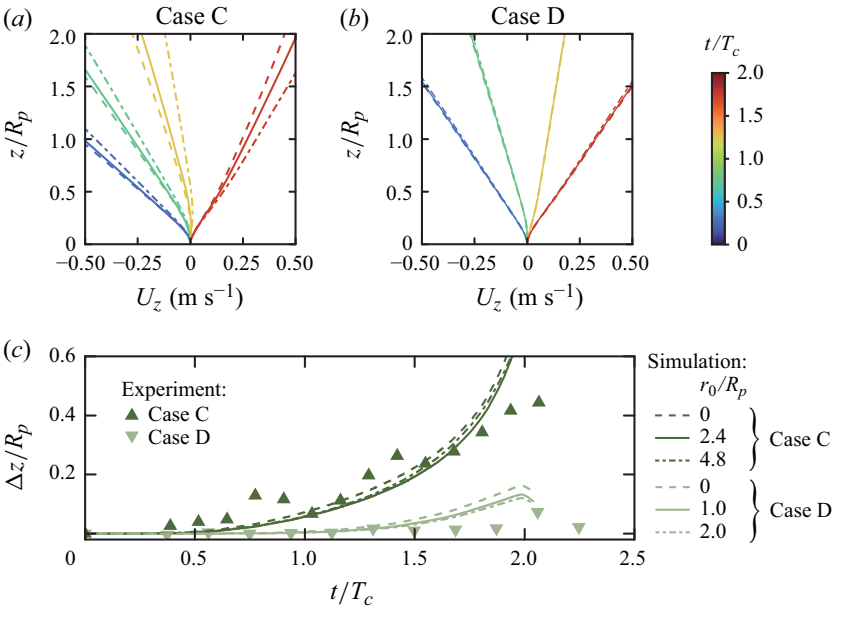


Figure 15. Influence of the initial radial offset on the motion of a PMMA particle ($R_p = 50\,\mu$m). (*a*) Profiles of undisturbed velocity U_z at $r/R_p = 0$ (dashed lines), $r/R_p = 2.4$ (solid lines) and $r/R_p = 4.8$ (dash-dotted lines) for case C ($\gamma = 1.3$, $R_{b,max}/R_p = 16$). (*b*) Profiles of undisturbed velocity U_z at $r/R_p = 0$ (dashed lines), $r/R_p = 1.0$ (solid lines) and $r/R_p = 2.0$ (dash-dotted lines) for case D ($\gamma = 1.8$, $R_{b,max}/R_p = 11$). (*c*) Simulated particle displacements for cases C and D at different r_0/R_p, compared with experiments (case C, $\gamma = 1.3 \pm 0.2$, $R_{b,max}/R_p = 15 \pm 1$, $r_0/R_p = 2.3$; case D, $\gamma = 1.8 \pm 0.1$, $R_{b,max}/R_p = 11 \pm 1$, $r_0/R_p = 1.0$). In (*a*) and (*b*), the colour bar on the right denotes the dimensionless time t/T_c for each case. In (*a*), the times t/T_c are 0.26, 0.75, 1.25 and 1.74; in (*b*), the times t/T_c are 0.29, 0.77, 1.26 and 1.74.

Both fits are valid for $\gamma^{partial} \in (0.5, 2.1)$ and $w/R_{b,max}^{partial} \in (0.4, 2.1)$. The fitting processes yield adjusted R-squared values 0.9480 for (A1), and 0.9045 for (A2). For bubble–particle interaction experiments with restricted fields of view, the bubble parameters obtained from the partial-boundary fitting method are converted to their corresponding full-boundary values using the relations given in (A1) and (A2).

Appendix B. Influence of the initial radial offset on particle vertical motion

An out-of-plane radial offset increases the effective radial offset of the particle. We therefore investigate its influence on particle vertical motion by comparing profiles of the undisturbed wall-normal velocity U_z at different radial distances r to the symmetrical axis for cases C and D in simulation, as shown in figures 15(*a*) and 15(*b*).

For case C ($\gamma = 1.3$), velocity profiles are distinguished by line types at selected distances $r/R_p = 0$, 2.4 and 4.8, and by colours at four selected times. The profiles at $r/R_p = 0$ and 2.4 are similar at each time instance, while the profiles at $r/R_p = 4.8$ exhibit higher velocity in the front stagnation flow, and lower velocity in the rear stagnation flow. For case D ($\gamma = 1.8$), all profiles at $r/R_p = 0$, 1.0 and 2.0 are similar at each selected time. With the flow fields at different radial distances, the simulated particle motions show little variation for both cases, with good agreement with the experimental data; see figure 15(*c*). Exemplified by case C with $r_0/R_p \lesssim 4.8$ ($r_0/R_{b,max} \lesssim 0.3$) and case D with $r_0/R_p \lesssim 2.0$ ($r_0/R_{b,max} \lesssim 0.2$), the results indicate that the initial radial offset has a limited influence on the particle vertical motion when $r_0/R_{b,max} \ll 1$ is satisfied.

https://doi.org/10.1017/jfm.2025.10998 Published online by Cambridge University Press

Appendix C. Estimation of the characteristic particle Reynolds number

To estimate the order of magnitude of Re_p, we consider typical values: $R_p \lesssim 250\,\mu\text{m}$, $\rho_l = 1 \times 10^3\ \text{kg m}^{-3}$ and $\mu_l = 1 \times 10^{-3}$ Pa s. The magnitude of $\|\boldsymbol{U} - \boldsymbol{v}_p\|$ is approximated by the vertical component of the flow field velocity at the particle's initial position ($r = 0$, $z = R_p$), which is

$$U_z|_{(r=0,\ z=R_p)} = R_b^2 \dot{R}_b \left[-\frac{1}{\left(L - R_p\right)^2} + \frac{1}{\left(L + R_p\right)^2} \right]. \tag{C1}$$

From $L \gg R_p$, we have

$$U_z|_{(r=0,\ z=R_p)} \approx -4 R_b^2 \dot{R}_b \frac{R_p}{L^3}, \tag{C2}$$

with its order of magnitude estimated as

$$U_z|_{(r=0,\ z=R_p)} \sim 4 R_{b,max}^2 \sqrt{\frac{\Delta p}{\rho_l}} \frac{R_p}{L^3} = 4 \sqrt{\frac{\Delta p}{\rho_l}} \frac{R_p}{R_{b,max}} \frac{1}{\gamma^3}. \tag{C3}$$

Substituting $R_{b,max}/R_p = 10$ and $\gamma = 2$ into (2.9) yields $Re_p \lesssim 250$. Therefore, (2.10) can be applied.

Appendix D. Derivation of $B(t_0)$ for $f'(R_p) \to 0$

At $t = t_0$, from (3.30), we have

$$R_b \ddot{R}_b = -2 \dot{R}_b^2. \tag{D1}$$

Eliminating $\ddot{R}_b$ in (3.3) by using (D1), we express the bubble wall velocity as

$$\dot{R}_b|_{(t=t_0)} = \sqrt{\frac{2\,\Delta p}{\rho_l}}. \tag{D2}$$

Combining (D2) and (3.25), we obtain

$$\left[\frac{3}{2\gamma} \left(\frac{R_b}{R_{b,max}} \right)^4 + 4 \left(\frac{R_b}{R_{b,max}} \right)^3 - 1 \right] \Bigg|_{(t=t_0)} = 0. \tag{D3}$$

The solution to (D3) depends on the dimensionless stand-off distance γ. Numerical calculations show that for the range of γ considered in this work (1.0–5.0), the solution for the dimensionless bubble radius at particle detachment from the solid wall $(R_b/R_{b,max})|_{(t=t_0)}$ falls within a narrow range (0.586, 0.621), and the non-dimensional time t_0/T_c ranges from 0.151 to 0.164. Therefore, within this range, we can approximate the solution with a constant, $(R_b/R_{b,max})|_{(t=t_0)} \approx 0.6$. Consequently, the estimated value of $B(t_0)$ is

$$B(t_0) = \frac{2\sqrt{2}\,(R_b/R_{b,max})|_{t=t_0}^2}{\gamma^3} \sqrt{\frac{\Delta p}{\rho_l}}\, R_{b,max}^{-1} \approx \frac{1.02}{\gamma^3} T_c^{-1}, \tag{D4}$$

which can be approximated as (3.31).

References

Annamalai, S. & Balachandar, S. 2017 Faxén form of time-domain force on a sphere in unsteady spatially varying viscous compressible flows. *J. Fluid Mech.* **816**, 381–411.

Arndt, R.E.A. 1981 Cavitation in fluid machinery and hydraulic structures. *Annu. Rev. Fluid Mech.* **13** (1), 273–328.

https://doi.org/10.1017/jfm.2025.10998 Published online by Cambridge University Press

ARORA, M., OHL, C.-D. & MØRCH, K.A. 2004 Cavitation inception on microparticles: a self-propelled particle accelerator. *Phys. Rev. Lett.* **92** (17), 174501.
BASSET, A.B. 1888 *Treatise on Hydrodynamics*. Deighton, Bell and Company.
BENJAMIN, T.B. & ELLIS, A.T. 1966 The collapse of cavitation bubbles and the pressures thereby produced against solid boundaries. *Phil. Trans. R. Soc. Lond. A* **260** (1110), 221–240.
BEST, J.P. & BLAKE, J.R. 1994 An estimate of the Kelvin impulse of a transient cavity. *J. Fluid Mech.* **261**, 75–93.
BORKENT, B.M., ARORA, M., C.-D., OHL, C.-D., DE JONG, N., VERSLUIS, M., LOHSE, D., MØRCH, K.A., KLASEBOER, E. & KHOO, B.C. 2008 The acceleration of solid particles subjected to cavitation nucleation. *J. Fluid Mech.* **610**, 157–182.
BOUSSINESQ, J. 1885 Sur la résistance qu'oppose un liquide indéfini en repos. *C. R. Acad. Sci. Paris* **100**, 935–937.
BRACKBILL, J.U., KOTHE, D.B. & ZEMACH, C. 1992 A continuum method for modeling surface tension. *J. Comput. Phys.* **100** (2), 335–354.
BRENNEN, C.E. 2014 *Cavitation and Bubble Dynamics*. Cambridge University Press.
BRUJAN, E.A., KEEN, G.S., VOGEL, A. & BLAKE, J.R. 2002 The final stage of the collapse of a cavitation bubble close to a rigid boundary. *Phys. Fluids* **14** (1), 85–92.
BULAT, T.J. 1974 Macrosonics in industry. *Ultrasonics* **12** (2), 59–68.
CHAHINE, G.L., KAPAHI, A., CHOI, J.-K. & HSIAO, C.-T. 2016 Modeling of surface cleaning by cavitation bubble dynamics and collapse. *Ultrason. Sonochem.* **29**, 528–549.
CHEN, D., QIU, M., LIN, Z., LIU, Q., ZHANG, G. & ZHU, Z. 2021 Experimental study on the interaction of a cavitation bubble flanked by two particles. *Acta Mech.* **232** (12), 4801–4810.
CLIFT, R., GRACE, J.R. & WEBER, M.E. 1978 *Bubbles, Drops and Particles*. Dover Publications.
DIJKINK, R. & OHL, C.-D. 2008 Measurement of cavitation induced wall shear stress. *Appl. Phys. Lett.* **93** (25), 254107.
DVORSKY, R., LUNACEK, J. & SLIVA, A. 2011 Dynamics analysis of cavitation disintegration of microparticles during nanopowder preparation in a new water jet mill (WJM) device. *Adv. Powder Technol.* **22** (5), 639–643.
GONZALEZ-AVILA, S.R., HUANG, X., QUINTO-SU, P.A., WU, T. & OHL, C.-D. 2011 Motion of micrometer sized spherical particles exposed to a transient radial flow: attraction, repulsion, and rotation. *Phys. Rev. Lett.* **107** (7), 074503.
HARRISON, M. 1952 An experimental study of single bubble cavitation noise. *J. Acoust. Soc. Am.* **24** (6), 776–782.
HOMANN, F. 1936 Der Einfluss grosser Zähigkeit bei der Strömung um den Zylinder und um die Kugel. *Z. Angew. Math. Mech.* **16** (3), 153–164.
HUANG, X., REN, C.-Z., LIU, P.-B. & HU, H.-B. 2024 On the interaction between a pulsating bubble and a particle on the rigid wall. *Phys. Fluids* **36** (10), 103301.
KARIMI, A. & MARTIN, J.L. 1986 Cavitation erosion of materials. *Intl Metals Rev.* **31** (1), 1–26.
KOCH, M., LECHNER, C., REUTER, F., KÖHLER, K., METTIN, R. & LAUTERBORN, W. 2016 Numerical modeling of laser generated cavitation bubbles with the finite volume and volume of fluid method, using OpenFOAM. *Comput. Fluids* **126**, 71–90.
KOLOMENSKIY, D. & MOFFATT, H.K. 2012 Similarity solutions for unsteady stagnation point flow. *J. Fluid Mech.* **711**, 394–410.
LAUTERBORN, W. & BOLLE, H. 1975 Experimental investigations of cavitation-bubble collapse in the neighbourhood of a solid boundary. *J. Fluid Mech.* **72** (2), 391–399.
LAUTERBORN, W. & OHL, C.-D. 1997 Cavitation bubble dynamics. *Ultrason. Sonochem.* **4** (2), 65–75.
LI, Q., ABBAS, M., MORRIS, J.F., CLIMENT, E. & MAGNAUDET, J. 2020 Near-wall dynamics of a neutrally buoyant spherical particle in an axisymmetric stagnation point flow. *J. Fluid Mech.* **892**, A32.
LI, S. 2006 Cavitation enhancement of silt erosion – an envisaged micro model. *Wear* **260** (9), 1145–1150.
LI, S., ZHANG, A.-M., WANG, S. & HAN, R. 2018 Transient interaction between a particle and an attached bubble with an application to cavitation in silt-laden flow. *Phys. Fluids* **30** (8), 082111.
MAXEY, M.R. & RILEY, J.J. 1983 Equation of motion for a small rigid sphere in a nonuniform flow. *Phys. Fluids* **26** (4), 883–889.
MORDYUK, B.N. & PROKOPENKO, G.I. 2004 Mechanical alloying of powder materials by ultrasonic milling. *Ultrasonics* **42** (1–9), 43–46.
OBRESCHKOW, D., BRUDERER, M. & FARHAT, M. 2012 Analytical approximations for the collapse of an empty spherical bubble. *Phys. Rev. E* **85** (6), 066303.
OHL, C.-D., ARORA, M., DIJKINK, R., JANVE, V. & LOHSE, D. 2006 Surface cleaning from laser-induced cavitation bubbles. *Appl. Phys. Lett.* **89** (7), 074102.

https://doi.org/10.1017/jfm.2025.10998 Published online by Cambridge University Press

OSEEN, C.W. 1927 *Hydrodynamik*. Akademische Verlagsgesellschaft.
PLESSET, M.S. 1949 The dynamics of cavitation bubbles. *ASME J. Appl. Mech.* **16** (3), 277–282.
POULAIN, S., GUENOUN, G., GART, S., CROWE, W. & JUNG, S. 2015 Particle motion induced by bubble cavitation. *Phys. Rev. Lett.* **114** (21), 214501.
RATTRAY, M. 1951 Perturbation effects in cavitation bubble dynamics. PhD thesis, California Institute of Technology.
RAYLEIGH, LORD 1917 VIII. On the pressure developed in a liquid during the collapse of a spherical cavity. *Phil. Mag.* **34** (200), 94–98.
REN, Z., LIU, S., TAN, B.H., DENNER, F., EVRARD, F., VAN WACHEM, B., ZUO, Z. & OHL, C.-D. 2021 Strong shear flows release gaseous nuclei from surface micro- and nanobubbles. *Phys. Rev. Fluids* **6** (4), 043601.
REN, Z., ZUO, Z., WU, S. & LIU, S. 2022 Particulate projectiles driven by cavitation bubbles. *Phys. Rev. Lett.* **128** (4), 044501.
REUTER, F., ZENG, Q. & OHL, C.-D. 2022 The Rayleigh prolongation factor at small bubble to wall stand-off distances. *J. Fluid Mech.* **944**, A11.
RUSCHE, H. 2002 Computational fluid dynamics of dispersed two-phase flow at high phase fractions. PhD thesis, University of London.
VIGOLO, D., GRIFFITHS, I.M., RADL, S. & STONE, H.A. 2013 An experimental and theoretical investigation of particle–wall impacts in a T-junction. *J. Fluid Mech.* **727**, 236–255.
VIGOLO, D., RADL, S. & STONE, H.A. 2014 Unexpected trapping of particles at a T junction. *Proc. Natl Acad. Sci. USA* **111** (13), 4770–4775.
WANG, J., LI, S., GU, J. & ZHANG, A.-M. 2023 Particle propulsion from attached acoustic cavitation bubble under strong ultrasonic wave excitation. *Phys. Fluids* **35** (4), 042009.
WANG, X., ZHANG, C., SU, H., LI, S., SHEN, J., ZHANG, Y., LI, J. & ZHANG, Y. 2024 Research on cavitation bubble behaviors between a dual-particle pair. *Phys. Fluids* **36** (2), 023310.
WU, S., LI, B., ZUO, Z. & LIU, S. 2021 Dynamics of a single free-settling spherical particle driven by a laser-induced bubble near a rigid boundary. *Phys. Rev. Fluids* **6** (9), 093602.
WU, S., ZUO, Z., STONE, H.A. & LIU, S. 2017 Motion of a free-settling spherical particle driven by a laser-induced bubble. *Phys. Rev. Lett.* **119** (8), 084501.
XIANG, G., CHEN, J., HO, D., SANKIN, G., ZHAO, X., LIU, Y., WANG, K., DOLBOW, J., YAO, J. & ZHONG, P. 2023 Shock waves generated by toroidal bubble collapse are imperative for kidney stone dusting during Holmium:YAG laser lithotripsy. *Ultrason. Sonochem.* **101**, 106649.
XU, P., LI, B., REN, Z., LIU, S. & ZUO, Z. 2023 Dynamics of a laser-induced buoyant bubble near a vertical rigid boundary. *Phys. Rev. Fluids* **8** (8), 083601.
ZENG, Q., AN, H. & OHL, C.-D. 2022 Wall shear stress from jetting cavitation bubbles: influence of the stand-off distance and liquid viscosity. *J. Fluid Mech.* **932**, A14.
ZENG, Q., GONZALEZ-AVILA, S.R., DIJKINK, R., KOUKOUVINIS, P., GAVAISES, M. & OHL, C.-D. 2018*a* Wall shear stress from jetting cavitation bubbles. *J. Fluid Mech.* **846**, 341–355.
ZENG, Q., GONZALEZ-AVILA, S.R., VOORDE, S.T. & OHL, C.-D. 2018*b* Jetting of viscous droplets from cavitation-induced Rayleigh–Taylor instability. *J. Fluid Mech.* **846**, 916–943.
ZENG, Q., ZHANG, A.-M., TAN, B.H., AN, H. & OHL, C.-D. 2024 Jetting enhancement from wall-proximal cavitation bubbles by a distant wall. *J. Fluid Mech.* **987**, R2.
ZHENG, X., WANG, X., LU, X., YUAN, J., ZHANG, Y. & ZHANG, Y. 2023 Experimental research on the collapse dynamics of the cavitation bubble near two spherical particles. *J. Mech. Sci. Technol.* **37** (5), 2451–2460.
ZHONG, P. 2013 Shock wave lithotripsy. In *Bubble Dynamics and Shock Waves* (ed. C.F. Delale), pp. 291–338. Springer.

https://doi.org/10.1017/jfm.2025.10998 Published online by Cambridge University Press